



|                              |  |
|------------------------------|--|
| <b>Publication Year</b>      | 2018   |
| <b>Acceptance in OA@INAF</b> | 2020-10-27T15:55:05Z   |
| <b>Title</b>                 | MIKiS: The Multi-instrument Kinematic Survey of Galactic Globular Clusters. I. Velocity Dispersion Profiles and Rotation Signals of 11 Globular Clusters |
| <b>Authors</b>               | Ferraro, F. R.; Mucciarelli, A.; Lanzoni, B.; Pallanca, C.; Lapenna, E.; et al.  |
| <b>DOI</b>                   | 10.3847/1538-4357/aabe2f   |
| <b>Handle</b>                | <a href="http://hdl.handle.net/20.500.12386/28029">http://hdl.handle.net/20.500.12386/28029</a>  |
| <b>Journal</b>               | THE ASTROPHYSICAL JOURNAL  |
| <b>Number</b>                | 860  |



# MIKIS: The Multi-instrument Kinematic Survey of Galactic Globular Clusters. I. Velocity Dispersion Profiles and Rotation Signals of 11 Globular Clusters\*

F. R. Ferraro<sup>1,2</sup> , A. Mucciarelli<sup>1,2</sup> , B. Lanzoni<sup>1,2</sup> , C. Pallanca<sup>1,2</sup> , E. Lapenna<sup>1,2</sup> , L. Origlia<sup>2</sup> , E. Dalessandro<sup>2</sup> , E. Valenti<sup>3</sup> , G. Beccari<sup>3</sup> , M. Bellazzini<sup>2</sup> , E. Vesperini<sup>4</sup> , A. Varri<sup>5</sup> , and A. Sollima<sup>2</sup>

<sup>1</sup> Dipartimento di Fisica e Astronomia, Università degli Studi di Bologna, via Gobetti 93/2, I-40129 Bologna, Italy

<sup>2</sup> INAF-Osservatorio di astrofisica e scienza dello spazio di Bologna, Via Gobetti 93/3, I-40129, Bologna, Italy

<sup>3</sup> European Southern Observatory, Karl-Schwarzschild-Strasse 2, D-85748 Garching bei München, Germany

<sup>4</sup> Department of Astronomy, Indiana University, Bloomington, IN, 47401, USA

<sup>5</sup> Institute for Astronomy, University of Edinburgh, Royal Observatory, Blackford Hill, Edinburgh EH9 3HJ, UK

Received 2018 February 9; revised 2018 April 10; accepted 2018 April 10; published 2018 June 11

## Abstract

We present the first results of the Multi-Instrument Kinematic Survey of Galactic Globular Clusters (GGCs), a project aimed at exploring the internal kinematics of a representative sample of GGCs from the radial velocity of individual stars, covering the entire radial extension of each system. This is achieved by exploiting the formidable combination of multi-object and integral field unit spectroscopic facilities of the ESO Very Large Telescope. As a first step, here we discuss the results obtained for 11 clusters from high and medium resolution spectra acquired through a combination of FLAMES and KMOS observations. We provide the first kinematical characterization of NGC 1261 and NGC 6496. In all the surveyed systems, the velocity dispersion profile declines at increasing radii, in agreement with the expectation from the King model that best fits the density/luminosity profile. In the majority of the surveyed systems, we find evidence of rotation within a few half-mass radii from the center. These results are in general overall agreement with the predictions of recent theoretical studies, suggesting that the detected signals could be the relic of significant internal rotation set at the epoch of the cluster's formation.

**Key words:** globular clusters: general – stars: kinematics and dynamics – techniques: spectroscopic

## 1. Introduction

Galactic globular clusters (GGCs) are the only astrophysical systems that, within the timescale of the age of the universe, undergo nearly all the physical processes known in stellar dynamics (Meylan & Heggie 1997; Heggie & Hut 2003). Gravitational interactions among stars significantly alter the overall energy budget and considerably affect the (otherwise normal) stellar evolution, even generating exotic objects like blue straggler stars, millisecond pulsars, X-ray binaries, and cataclysmic variables (e.g., Bailyn 1995). Hence GGCs represent ideal laboratories in which to study stellar dynamics and its effects on stellar evolution. Traditionally, GCs have been assumed to be quasi-relaxed nonrotating systems, characterized by spherical symmetry and orbital isotropy. Hence, spherical, isotropic, and nonrotating models, with a truncated distribution function close to a lowered-Maxwellian (e.g., King 1966), have been routinely used to fit the observed surface brightness profiles and estimate the main GC structural parameters, like the core and half-mass radii, the concentration and even the total mass (Pryor & Meylan 1993; Harris 1996; McLaughlin & van der Marel 2005). While accurate cluster structural parameters are now being derived from a new generation of star density profiles (see Ferraro et al. 2009; Lanzoni et al. 2010; Dalessandro et al. 2013a; Miocchi et al. 2013), this information alone is not sufficient to univocally constrain the models and get a comprehensive view of GC physics (Meylan & Heggie 1997). The crucial missing ingredient is the information about cluster internal dynamics.<sup>6</sup> In particular,

a detailed knowledge of the velocity dispersion (VD) profile and the (possible) rotation curve of GGCs is still missing in the majority of the cases. This is essentially due to observational difficulties.

In principle, VD and rotation can be obtained from different approaches. One is to use the line broadening and the shift of integrated-light spectra (e.g., Ibata et al. 2009; Lützgendorf et al. 2011, 2013; Fabricius et al. 2014). However, in the case of resolved stellar populations like GGCs, this method can be prone to a severe “shot noise bias” (Dubath et al. 1997; Lanzoni et al. 2013). In fact, if a few bright giants bring a dominant contribution into the integrated-light spectrum, the line broadening provides a measure of their radial velocity (RV) scatter, instead of a measure of the cluster VD due to the underlying stellar population. The other approaches consist of determining the cluster VD from the velocities of statistically significant samples of individual stars, either through resolved spectroscopy, thus obtaining the line-of-sight VD (e.g., Lane et al. 2010; Bellazzini et al. 2012; Bianchini et al. 2013; Husser et al. 2016; Baumgardt 2017; Baumgardt & Hilker 2018; Kamann et al. 2018), or via internal proper motions, which provide the two VD components on the plane of the sky (see, e.g., Bellini et al. 2014 for recent results). The latter is very challenging since it requires high-precision photometry and astrometry on quite long time baselines and it just started to be feasible, mainly thanks to the combination of first and second epoch *HST* observations and the improved techniques of data analysis (see Bellini et al. 2014, 2017; Watkins et al. 2015, and the Gaia Survey). RVs are, in principle, easier to obtain (through spectroscopy) and measurable in any cluster region and in GCs at any distance from Earth within the Galaxy. However, determining the line-of-sight VD profile from individual stars over the entire cluster extension is hard and

\* Based on FLAMES and KMOS observations performed at the European Southern Observatory as part of the Large Programme 193.D-0232 (PI: Ferraro).

<sup>6</sup> Recent results suggest that insights on GC internal dynamics can be obtained from the observations of exotic stellar populations, like blue stragglers and millisecond pulsars (Ferraro et al. 2009, 2012; Lanzoni et al. 2016).

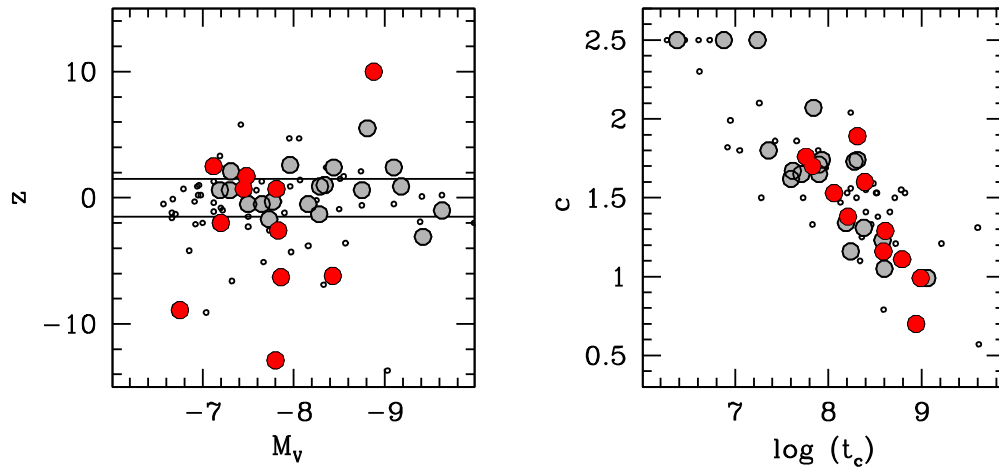


**Figure 1.** Distribution of the GGCs observed in the MikiS survey (large circles) in the planes of height on the Galactic plane vs. absolute integrated  $V$ -band magnitude (left) and concentration parameter vs. core relaxation time (right). The 11 clusters discussed here are in red. The entire GGC population is also plotted for reference (small dots).

very telescope time consuming, since it requires us to collect large samples of individual stellar spectra both in environments of high stellar crowding (up to  $\sim 7 \times 10^5 L_\odot \text{ pc}^{-3}$ ; see Harris 1996, 2010 version) and over large sky regions (of  $20'$ – $40'$  diameter and even more).

To overcome these obstacles, we recently proposed the combination of spectroscopic observations acquired from multiple instruments with different multi-object capabilities and different angular resolution powers. In this paper, we present first results obtained from the proposed approach. Section 2 provides an overview of our multi-instrument survey. In Section 3, we describe the observations and the adopted data reduction procedures. The determination of the stellar RVs and the homogenization of the different data sets is discussed in Section 4. The results are presented in Section 5, while Sections 6 and 7 are devoted to the discussion and conclusions.

## 2. The MikiS Survey

The Multi-Instrument Kinematic Survey of GGCs (hereafter, the MikiS survey) was specifically designed to provide the entire VD and rotation profiles of a representative sample of GGCs by fully exploiting the spectroscopic capabilities available at the ESO Very Large Telescope (VLT). The core scheme of the survey is to take advantage of the specific characteristics of three different VLT spectrographs: (1) the diffraction-limited integral field (IF) spectrograph SINFONI, which allows us to resolve GC stars in the innermost few arcseconds from the center; (2) the seeing-limited IF spectrograph KMOS, which provides an optimal coverage of the intermediate radial range (tens of arcsecond scale), and (3) the wide-field multi-object spectrograph FLAMES, which samples the external cluster regions (out to a dozen arcminutes) with more than 100 fibers simultaneously. This approach was first tested, as a proof of concept, for the case of NGC 6388 (Lanzoni et al. 2013; Lapenna et al. 2015b).

For the MikiS survey, we selected a sample of 30 GCs that are well representative of the overall Galactic population (see Figure 1): they properly encompass (i) the cluster dynamically sensitive parameter space (spanning a large range of central

densities and a factor of 3 in the concentration parameter), (ii) different stages of dynamical evolution (the sample includes both pre- and post-core-collapse GCs, with the core relaxation time spanning almost 3 orders of magnitude), and (iii) different environmental conditions (they are distributed at different heights on the Galactic plane, thus sampling both the bulge/disk and the halo populations:  $|z| < 1.5 \text{ kpc}$  and  $1.5 < |z| < 13$ , respectively). The selected targets are also more luminous than  $M_V = -6.8$  (i.e., populous enough to guarantee large samples of giant stars for a meaningful determination of the VD), relatively close to Earth (within  $\sim 16 \text{ kpc}$ , thus providing spectra with good signal-to-noise ratios (S/Ns) for stars down to the sub-giant branch, in reasonable exposure times) and not extremely metal-poor ( $[\text{Fe}/\text{H}] > -1.8$ , thus allowing RV measurements with an accuracy of a few kilometers per second also from relatively low-resolution IR spectra).

Thanks to the adopted strategy and the selected cluster sample, the MikiS survey is expected to provide the full characterization of the line-of-sight internal kinematics from the innermost to the outermost regions of each cluster, with crucial impact on many hot topics of GC science. We will properly search for signatures of systemic rotation and intermediate-mass ( $10^3$ – $10^4 M_\odot$ ) black holes, thus providing new crucial insights on the physics and formation processes of both GCs and these elusive compact objects (see, e.g., Baumgardt et al. 2005; Miocchi 2007; Varri & Bertin 2012; Tiongco et al. 2017; Zocchi et al. 2017). We will also accurately determine the whole mass distribution and the global amount of dark remnants (white dwarfs, neutron stars, and stellar mass black holes) in the sampled clusters. While a complete census of these stars is beyond any observational possibility, the VD profile is sensitive to the whole mass enclosed in a stellar orbit. Hence, the simultaneous knowledge of the density and the VD profiles can provide reliable estimates of the stellar densities, mass-to-light ratios, and cluster total mass (Mandushev et al. 1991; Pryor & Meylan 1993; Meylan & Heggie 1997; Lane et al. 2010; Sollima et al. 2012; Zocchi et al. 2012; Baumgardt 2017; Baumgardt & Sollima 2017). We also aim at characterizing the kinematics of multiple populations with different light-element content, to

**Table 1**  
Number and Duration of the Exposures Secured for Each Cluster within the MikiS Survey

| CLUSTER  |     | FLAMES            |                   |                   | KMOS            |                  |
|----------|-----|-------------------|-------------------|-------------------|-----------------|------------------|
| NGC 288  |     | $2 \times 1770$ s | $1 \times 2670$ s |                   | $2 \times 60$   | $1 \times 100$ s |
| NGC 362  |     | $1 \times 900$ s  | $2 \times 1770$ s | $7 \times 30$ s   |                 | $4 \times 100$ s |
| NGC 1261 |     | $2 \times 1770$ s | $2 \times 2670$ s |                   |                 | $5 \times 100$ s |
| NGC 1904 | M79 | $2 \times 2670$ s |                   | $2 \times 30$ s   |                 | $2 \times 100$ s |
| NGC 3201 |     | $1 \times 900$ s  | $3 \times 1770$ s | $6 \times 30$ s   | $2 \times 60$   | $2 \times 100$ s |
| NGC 5272 | M3  | $1 \times 900$ s  | $3 \times 1800$ s | $2 \times 2670$ s | $8 \times 30$ s | $2 \times 100$ s |
| NGC 5927 |     | $4 \times 1800$ s | $1 \times 2670$ s | $4 \times 30$ s   |                 | $5 \times 100$ s |
| NGC 6171 |     | $2 \times 900$ s  | $1 \times 1800$ s | $1 \times 2700$ s | $5 \times 60$   | $2 \times 100$ s |
| NGC 6254 | M10 | $1 \times 1200$ s | $1 \times 1331$ s | $2 \times 1800$ s | $4 \times 30$ s | $2 \times 100$ s |
| NGC 6496 |     | $3 \times 1800$ s | $1 \times 2700$ s | $1 \times 5400$ s |                 | $5 \times 300$ s |
| NGC 6723 |     | $3 \times 900$ s  | $3 \times 1800$ s | $1 \times 2700$ s | $5 \times 30$ s | $4 \times 100$ s |

provide crucial constraints to GC formation scenarios (e.g., Richer et al. 2013; Vesperini et al. 2013; Bellini et al. 2015; Hénault-Brunet et al. 2015; Cordero et al. 2017). Finally, the MikiS survey will allow the exploration of GC dynamics in the proximity of their tidal limitation, which is essential in order to formulate more realistic descriptions of this class of stellar systems (e.g., Davoust 1977; McLaughlin & van der Marel 2005; Gieles & Zocchi 2015), to pin down the physical origin of recently claimed “extra-tidal” structures (e.g., see Olszewski et al. 2009; Correnti et al. 2011 and, more recently, Kuzma et al. 2016, 2018; Carballo-Bello et al. 2018), to investigate the interplay with the external tidal field (e.g., Heggie & Ramamani 1995; Varri & Bertin 2009), and even to assess the implications of more exotic possibilities such as small dark matter halos (e.g., Mashchenko & Sills 2005; Shin et al. 2013; Peñarrubia et al. 2017) or modifications of the theory of gravity (e.g., Ibata et al. 2011; Hernandez et al. 2013).

While a few works based on the data acquired with the MikiS survey have already been published on specific subtopics (Lapenna et al. 2015a; Ferraro et al. 2016; Sollima et al. 2016), this is the first paper of a series specifically devoted to discuss the kinematic results of the survey. As a first step, here we present the VD profiles and the rotation signals detected in the intermediate/outer regions of 11 GGCs (highlighted in red in Figure 1), which represent the bulk of the targets observed only with the FLAMES+KMOS combination. In a series of future studies we will discuss the most intriguing cases obtained from the combined use of the all three instruments (SINFONI+KMOS+FLAMES).

### 3. Observations and Data Reduction

Within the MikiS survey, we used FLAMES (Pasquini et al. 2000) in the GIRAFFE/MEDUSA combined mode (consisting of 132 deployable fibers that can be allocated within a  $25'$ -diameter field of view), adopting the HR21 grating setup, with a resolving power  $R \sim 16,200$  and a spectral coverage from 8484 to 9001 Å. This grating samples the prominent Ca II triplet lines, which are excellent features to measure RVs also in relatively low ( $\sim 10$ – $15$ ) S/N spectra. The target stars have been selected from optical wide-field photometric catalogs presented in previous papers (see, e.g., Ferraro et al. 2004, 2012; Lanzoni et al. 2007a, 2007b; Dalessandro et al. 2013a, 2013b). We selected only red giant branch stars brighter than  $I = 18.5$  and, in order to avoid spurious contamination from other sources within the fibers, we also requested that no bright neighbors ( $I_{\text{neighbor}} < I_{\text{star}} + 1.0$ ) were present within  $2''$  from

each target. On average, three to four pointings have been performed in each cluster. For each pointing, multiple exposures, with total integration times ranging from 900 to 3000 s according to the magnitude of the targets, were secured (see Table 1). This provided S/Ns  $\sim 30$  at the faintest magnitudes. For each target cluster, one pointing has been dedicated to reobserve 10–20 stars in common with the pre-existing data sets that we retrieved from the ESO archive (see Table 2) in order to increase at most the sample of individual FLAMES spectra. The data reduction was performed by using the FLAMES-GIRAFFE pipeline,<sup>7</sup> including bias-subtraction, flat-field correction, wavelength calibration with a standard Th–Ar lamp, resampling at a constant pixel-size and extraction of one-dimensional spectra. Typically, 15–20 fibers were used to measure the sky in each exposure. These spectra have been averaged to obtain a master sky spectrum, which was then subtracted from each target spectrum.

We have used KMOS (Sharples et al. 2010) to measure red giant stars with  $J < 14$ , located within  $\sim 70''$  from each cluster center. KMOS is a spectrograph equipped with 24 deployable IF units that can be allocated within a  $7.2'$  diameter field of view. Each IF unit covers a projected area on the sky of about  $2''.8 \times 2''.8$ , sampled by an array of  $14 \times 14$  spatial pixels (spaxels) with an angular size of  $0''.2$  each. We have used the YJ grating covering the  $1.00$ – $1.35 \mu\text{m}$  spectral range at a resolution  $R \approx 3400$ , corresponding to a sampling of about  $1.75 \text{ Å pixel}^{-1}$ , i.e.,  $\sim 46 \text{ km s}^{-1} \text{ pixel}^{-1}$  at  $1.15 \mu\text{m}$ . This instrumental setup is especially effective in simultaneously measuring a number of reference telluric lines in the spectra of giant stars, for an accurate calibration of the RV, despite the relatively low spectral resolution. Typically, seven to eight pointings have been secured in each cluster. The total on-source integration time for each pointing was 3–5 minutes and it has been obtained with three subexposures of 60–100 s each, dithered by  $0''.2$  for optimal flat-field correction. The typical S/N of the observed spectra is  $\gtrsim 50$ . We used the “nod to sky” KMOS observing mode and nodded the telescope to an off-set sky field at  $\approx 6'$  north of the cluster center, for a proper background subtraction. The spectroscopic targets have been selected from near-IR catalogs published by our group (Ferraro et al. 2000; Valenti et al. 2004, 2007), on the basis of their position in the color–magnitude diagrams. We selected red giant targets with  $J < 14$  mag and with no stars brighter than

<sup>7</sup> <http://www.eso.org/sci/software/pipelines/>



**Table 2**

Summary of the FLAMES Data Sets Used to Derive the Internal Kinematics of the Target GCs

| Cluster      | Program ID                      | Grating   |
|--------------|---------------------------------|-----------|
| NGC 288      | 074.A-0508 (PI Drinkwater)      | LR2-LR4   |
|              | 073.D-0211 (PI Carretta)        | HR11-HR13 |
|              | 075.D-0043 (PI Carraro)         | HR9       |
|              | 087.D-0276 (PI D’Orazi)         | HR15-HR19 |
|              | 088.B-0403 (PI Lucatello)       | HR9       |
|              | 193.D-0232 (PI Ferraro)         | HR21      |
| NGC 362      | 083.D-0208 (PI Carretta)        | HR11-HR13 |
|              | 087.D-0276 (PI D’Orazi)         | HR15N     |
|              | 088.D-0026 (PI Mc Donald)       | HR14-HR15 |
|              | 188.B-3002 (PI Gilmore)         | HR10-HR21 |
|              | 193.D-0232 (PI Ferraro)         | HR21      |
| NGC 1261     | 193.D-0232 (PI Ferraro)         | HR21      |
|              | 188.B-3002 (PI Gilmore)         | HR10-HR21 |
|              | 193.B-0936 (PI Gilmore)         | HR10-HR21 |
| NGC 1904 M79 | 072.D-0507 (PI Carretta)        | HR11-HR13 |
|              | 085.D-0205 (PI Carretta)        | HR21      |
|              | 193.B-0936 (PI Gilmore)         | HR10-HR21 |
|              | 193.D-0232 (PI Ferraro)         | HR21      |
| NGC 3201     | 171.B-0520 (PI Gilmore)         | LR8       |
|              | 073.D-0211 (PI Carretta)        | HR11-HR13 |
|              | 087.D-0276 (PI D’Orazi)         | HR15-HR19 |
|              | 088.B-0403 (PI Lucatello)       | HR9       |
|              | 193.D-0232 (PI Ferraro)         | HR21      |
| NGC 5272 M3  | 093.D-0536 (PI Contreras Ramos) | HR12      |
|              | 193.D-0232 (PI Ferraro)         | HR21      |
| NGC 5927     | 079.B-0721 (PI Feltzing)        | HR13      |
|              | 188.B-3002 (PI Gilmore)         | HR10-HR21 |
|              | 193.D-0232 (PI Ferraro)         | HR21      |
| NGC 6171     | 073.D-0211 (PI Carretta)        | HR13      |
|              | 193.D-0232 (PI Ferraro)         | HR21      |
|              | 071.D-0311 (PI Scarpa)          | HR9       |
| NGC 6254 M10 | 073.D-0211 (PI Carretta)        | HR11-HR13 |
|              | 193.B-0232 (PI Ferraro)         | HR21      |
| NGC 6496     | 193.D-0232 (PI Ferraro)         | HR21      |
| NGC 6723     | 087.D-0230 (PI Gratton)         | HR12-HR19 |
|              | 193.D-0232 (PI Ferraro)         | HR21      |

**Note.** For each system, the proposal ID, the PI, and the used grating are listed. The data sets acquired within the MikiS survey correspond to program ID 193.D-0232, while the others have been retrieved from the ESO archive.

$J = 15$  within  $1''$  from their center. We also used ACS-*HST* data in the F606W and F814W bands, from Sarajedini et al. (2007), to identify additional stars not present in the IR catalog. The raw data have been reduced using the KMOS pipeline,<sup>3</sup> which performs background subtraction, flat-field correction, and wavelength calibration of the 2D spectra. The 1D spectra have been extracted manually by visually inspecting each IF unit and selecting the spectrum from the brightest spaxel in correspondence with each target star centroid, in order to minimize the effects of possible residual contamination from nearby stars and/or from the unresolved stellar background. Normally, one star was measured in each IF unit. Only in a few cases were two or more resolved stars clearly distinguishable in a single KMOS IF unit, and their spectra were extracted.

## 4. RV Measurements

To measure the RVs of the target stars, we cross-correlated the observed spectra (corrected for heliocentric velocity) with a template of known velocity, following the procedure described in Tonry & Davis (1979) and implemented in the FXCOR software under IRAF. As templates, we used synthetic spectra computed with the SYNTH code (see, e.g., Sbordone et al. 2004), adopting the clusters metallicity and appropriate atmospheric parameters according to the evolutionary stage of the targets. All of the synthetic spectra have been convoluted with a Gaussian profile to reproduce the spectral resolution of each data set. Finally, a visual inspection of all the observed spectra shifted to zero velocity, compared with the synthetic template, has been performed to assess the quality of the solution.

For the FLAMES targets, we measured the RV in three different regions of the same spectrum (region 1:  $8490 \text{ \AA} < \lambda < 8630 \text{ \AA}$ , region 2:  $8630 \text{ \AA} < \lambda < 8770 \text{ \AA}$ , region 3:  $8790 \text{ \AA} < \lambda < 8900 \text{ \AA}$ ), each including a large number of lines. The star velocity and its uncertainty are then obtained, respectively, as the mean of these different measures, and their dispersion divided by the square root of the number of spectral regions used. The typical uncertainties in the RVs derived for FLAMES targets are of the order of  $0.1\text{--}0.3 \text{ km s}^{-1}$ . Before combining RV measurements obtained from different FLAMES gratings, we checked for possible systematic offsets. Since we adopted the RVs acquired in the MikiS survey as reference, for the stars observed with the HR21 setup, we checked the accuracy of the zero-point of the wavelength calibration by measuring the position of several emission sky lines available in the spectral range, finding no significant offsets. Then, in order to align the other FLAMES data sets, we used the stars in common (typically a dozen for each cluster), always finding a very good agreement. When multiple exposures were available for the same star, we first verified that RV measures agreed within the errors (if not, the star was assumed to be a candidate binary system and excluded from the analysis),<sup>8</sup> and we then determined its final RV as the weighted mean of all the measures, by using the individual errors as weights.

For the KMOS targets, the precision on the derived RVs has been estimated through Monte Carlo simulations, using cross-correlation against 500 synthetic spectra of a given S/N per pixel. The synthetic spectra have been calculated over the wavelength region covered by KMOS and assuming the appropriate metallicity of the cluster and the typical atmospheric parameters of the observed targets. Each synthetic spectrum has been resampled at the KMOS pixel-scale ( $1.75 \text{ pixel/\AA}$ ) and a Poissonian noise has been injected to reproduce a given S/N per pixel (we simulated S/Ns between 20 and 80). The dispersion of the derived RV distribution is adopted as the  $1\sigma$  uncertainty for a given S/N. An exponential relation between the S/N and the RV precision as estimated from the above procedure has been derived and used to attribute an RV error to each target. The final errors for KMOS RVs are typically of the order of  $1\text{--}5 \text{ km s}^{-1}$ .

<sup>8</sup> Operationally, we determined the scatter of the RV measures available for a given target and compared it to the rms of the error distribution of the stars with similar magnitude: if it was larger by a factor of 3 or more, then the target was classified as a candidate binary and excluded from the analysis. Clearly, this is just a zero-order selection and some binary system could still present in our samples. However, our observations are limited to the brightest portion of the color-magnitude diagram, essentially sampling the red giant branch, and we therefore expect no significant effects on the discussed results: in fact, binaries with red giant companions in GCs amount to a very small fraction ( $\lesssim 2\%$ ) and they show RV variations of just  $1\text{--}2 \text{ km s}^{-1}$  (see, e.g., Sommariva et al. 2009).

**Table 3**  
Observed Samples in the Program Clusters

| Cluster  | $N_{\text{obs}}$ | $r_{\text{min}}$<br>(arcsec) | $r_{\text{max}}$<br>(arcsec) | $N_{\text{memb}}$ |
|----------|------------------|------------------------------|------------------------------|-------------------|
| NGC 288  | 538              | 1.0                          | 853                          | 419               |
| NGC 362  | 717              | 1.0                          | 815                          | 543               |
| NGC 1261 | 320              | 1.2                          | 728                          | 299               |
| NGC 1904 | 235              | 3.8                          | 774                          | 173               |
| NGC 3201 | 587              | 4.7                          | 749                          | 454               |
| NGC 5272 | 628              | 1.9                          | 750                          | 577               |
| NGC 5927 | 851              | 5.2                          | 784                          | 534               |
| NGC 6171 | 482              | 3.0                          | 746                          | 319               |
| NGC 6254 | 565              | 9.8                          | 775                          | 415               |
| NGC 6496 | 656              | 8.6                          | 753                          | 234               |
| NGC 6723 | 696              | 2.1                          | 731                          | 487               |

**Note.** Total number of observed stars ( $N_{\text{obs}}$ ), minimum and maximum distances from the cluster center sampled by the RV data sets ( $r_{\text{min}}$  and  $r_{\text{max}}$ , respectively), and number of member stars used for the determination of the VD profile and the search for systemic rotation ( $N_{\text{memb}}$ ).

To homogenize the RV measurements obtained from FLAMES and KMOS, we used at least 10 targets per cluster that have been observed with both the spectrographs. The measured offsets ( $3\text{--}5\text{ km s}^{-1}$ ) can be explained by a combined effect of the relatively low spectral resolution of KMOS and the low metallicity of a few clusters (yielding to KMOS spectra with lower S/Ns). We then double-checked the realignment of the two data sets by comparing the systemic velocities (see Section 5.1) of the FLAMES and the KMOS samples separately in each GC. Finally, for each star in common between the two samples, we adopted the RV measure obtained from the (higher resolution) FLAMES spectra.

## 5. Results

### 5.1. Systemic Velocities

The total number of stars with measured RV in each program cluster is listed in Table 3, together with the minimum and the maximum distance from the center sampled by the collected data sets. The catalogs of the measured RVs are freely downloadable at the MikiS web page.<sup>9</sup> Figures 2–5 show the distribution of the measured RVs as a function of the distance from the cluster center. The data span a large range of radial distances from the central regions out to  $\sim 800''$ , extending, in some cases, even beyond the nominal cluster tidal radius. The population of cluster members is clearly distinguishable as a narrow, strongly peaked component, which dominates the sample at radii smaller than  $\sim 500''$ .

In a few clusters, the field component is clearly identified as a broad distribution at all sampled radii, homogeneously spanning a wide range of RVs (typically  $\sim 200\text{ km s}^{-1}$ ). Three systems (namely NGC 5927, NGC 6171, and NGC 6496) appear to be particularly affected by the tail of the field velocity distribution, which significantly overlaps that of the cluster. While this can impact the determination of the cluster VD and rotation (see Sections 5.3 and 5.4), it is not an issue for measuring the systemic velocity of the cluster ( $V_{\text{sys}}$ ). In fact, the latter has been obtained by conservatively considering only

stars with RVs in a relatively narrow strip of values (typically  $\Delta RV = \pm 20\text{ km s}^{-1}$ ) centered at the histogram peak velocity. We also excluded the most external radial bins, where the number of field stars can be comparable to (or even larger than) that of cluster members. Assuming that the RV distribution is Gaussian, we used a Maximum-Likelihood method (e.g., Walker et al. 2006, see also Section 5.3) to estimate its mean and uncertainty. The values of  $V_{\text{sys}}$  thus obtained for each cluster are listed in Table 4 and labeled in Figures 2–5. In the following, we will use  $\tilde{V}_r$  to indicate RVs referred to the cluster systemic velocity:  $\tilde{V}_r \equiv V_r - V_{\text{sys}}$ .

### 5.2. Cluster Membership

As discussed above, the cluster membership selection is straightforward in all the sampled systems except for three (namely NGC 5927, NGC 6171, and NGC 6496). Thus, before discussing the procedure adopted to determine the VD profile and to search for signals of systemic rotation, we describe the approach used to decontaminate these three systems. In principle, besides the RV values, an additional constrain to the cluster membership can be obtained from the stellar metallicity, provided that the two samples (cluster and Galactic field) have different [Fe/H] distributions. KMOS spectra can provide metallicities with uncertainties of about 0.2–0.3 dex, due to the low spectral resolution of the instrument (and the low metallicities of most of the program cluster). Moreover, the KMOS targets are located in the innermost cluster regions, where the field contamination is not critical. Hence, metallicities from KMOS spectra have not been used to distinguish cluster from field stars. Instead, for all the targets observed with the HR21 grating of FLAMES in the three most contaminated systems, we have estimated the [Fe/H] ratio from the Ca II triplet lines. The equivalent width has been measured by fitting the Ca II triplet profile with a Voigt function. Then, [Fe/H] values have been derived for most of the targets by adopting the relation of Vasquez et al. (2015), which is calibrated as a function of the K-band magnitude. For the stars with no K magnitude information, we used the relation of Carrera et al. (2007), which is calibrated in the V-band. The reference horizontal branch magnitudes adopted in this analysis are from Harris (1996). We checked that the two considered relations are consistent and the derived metallicities are compatible within the measure uncertainties ( $\sim 0.1\text{--}0.12$  dex).

Figure 6 shows the measured metallicity as a function of RV. It is apparent that cluster members clump in restricted ranges of RV and [Fe/H] values (in agreement with the literature, the metallicities are centered at [Fe/H] =  $-0.49$ ,  $-1.06$ , and  $-0.56$  in NGC 5927, NGC 6171, and NGC 6496, respectively, and have intrinsic dispersions of the same order of the uncertainties; e.g., Harris 1996). Instead, field stars have much larger scatters. Unfortunately, the metallicity distribution of the field largely overlaps that of the three clusters (the most favorable case being NGC 6171), and it therefore does not allow us to implement a conclusive separation between the two components. We therefore performed just a first-order decontamination by excluding from the following kinematical analysis all the stars with metallicity below and above the cluster values (which are marked by the two dashed lines in each panel of Figure 6). Clearly, this leaves a sample of stars (either having [Fe/H] compatible with the cluster value, or with no metallicity information) that still include field contaminants, with an RV distribution partially overlapping that of genuine cluster

<sup>9</sup> [http://www.cosmic-lab.eu/Cosmic-Lab/Cosmic-Lab/FLAMES\\_KMOS.html](http://www.cosmic-lab.eu/Cosmic-Lab/Cosmic-Lab/FLAMES_KMOS.html)

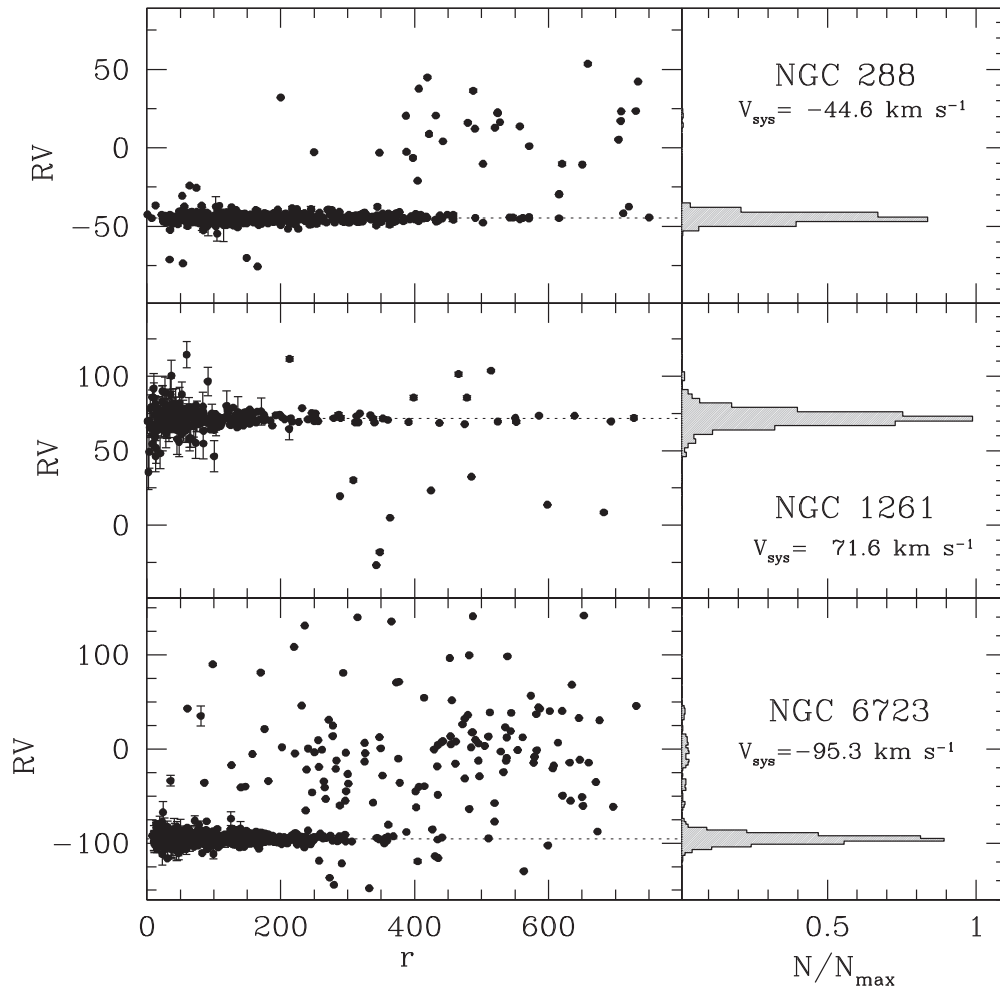


**Figure 2.** Left panels: Radial velocities as a function of the distance from the cluster center obtained from the KMOS+FLAMES observations of NGC 288, NGC 1261, and NGC 6723 (see labels). RVs are in kilometers per second, radial distances are in arcseconds. Right panels: histogram of the corresponding RV distribution, with the value of the derived systemic velocity labeled for each cluster. The histograms are normalized to their peak values.

members. To remove such a residual field contamination, we thus adopted the double-Gaussian statistical approach described below.

### 5.3. VD Profile

The projected VD profile,<sup>10</sup>  $\sigma_P(r)$ , has been determined from the measured RVs by splitting the surveyed area in a set of concentric annuli, chosen as a compromise between a good radial sampling and a statistically significant number ( $\gtrsim 40$ ) of stars.<sup>11</sup> In each radial bin, obvious outliers (i.e., stars with RVs in clear disagreement with the cluster distribution in that radial interval) have been excluded from the analysis and a  $3\sigma$ -clipping selection about the cluster systemic velocity has been used to further clean the sample. Then,  $\sigma_P(r)$  has been computed from the dispersion of the remaining  $\tilde{V}_r$  values following the Maximum-Likelihood method described in Walker et al. (2006, see also Martin et al. 2007; Sollima

et al. 2009). Errors have been estimated following Pryor & Meylan (1993).

For the three most contaminated clusters, we assumed that the RV distribution of the stars that survived the metallicity selection (see Section 5.2) is the combination of two Gaussian functions, one representing the cluster contribution, the other corresponding to the field. Obviously, the cluster Gaussian is peaked at  $V_{\text{sys}}$  and its dispersion varies from one bin to another following the VD profile. Instead, the Gaussian function corresponding to foreground/background stars in the direction of each cluster is peaked at the characteristic velocity of the Galactic field in that region, and has a much larger dispersion. To determine the peak and the dispersion values of the field Gaussian, we used the RV distribution of the stars observed at large distances from the cluster center, where the field is largely dominant with respect to the cluster. Under the assumption that the observed RV distribution has a double-Gaussian profile, we thus used the same Maximum-Likelihood method described above to determine the cluster VD from the dispersion of the cluster Gaussian function (see Sollima et al. 2016 for more details).

The resulting VD profiles are shown in Figure 7 and listed in Table 5. For NGC 1261 and NGC 6496, these are the first determinations in the literature. Three clusters (namely NGC 362, NGC 3201, and NGC 6254) are in common with the sample recently published by Kamann et al. (2018), who used

<sup>10</sup> Formally, the derived values of  $\sigma_P(r)$  are the second moments of the RV distribution, which coincide with the true VD only in the case of null rotation. However, as discussed below (Section 6), the rotational velocity always provides a negligible contribution, and this measure can therefore be assumed as the true stellar VD.

<sup>11</sup> The number of stars per bin can be lower than 40 in the most external annulus of a few clusters because of the intrinsic outward density decline, and in NGC 1904 because only 235 RVs in total are available for this system.

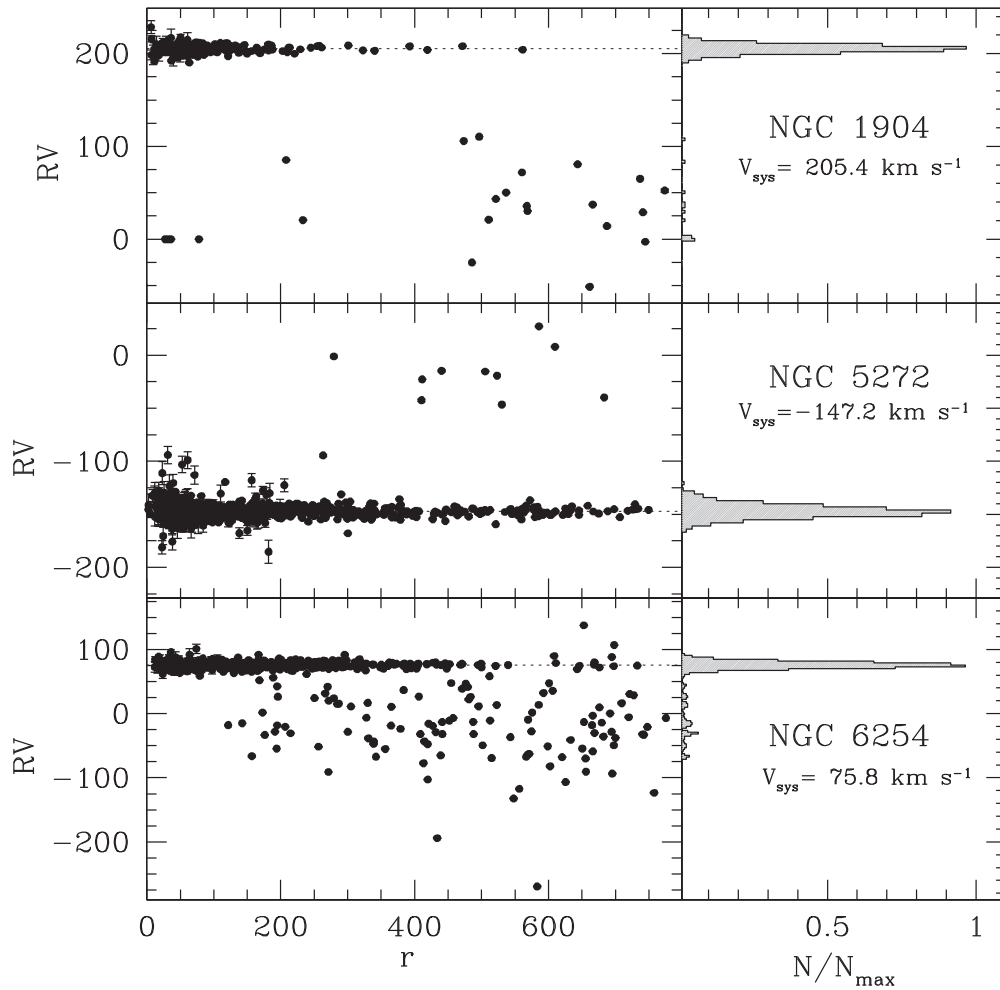


**Figure 3.** As in Figure 2, but for NGC 1904, NGC 5272, and NGC 6254.

the IF spectrograph MUSE to survey the central regions of 25 GCs. The comparison between the VD profiles obtained in the present work and in Kamann et al. (2018) for these three systems (Figure 8) shows a good agreement in the radial region in common, and clearly illustrates that the two studies are well complementary, with the MUSE data covering distances out to  $\sim 50''$ , while our KMOS+FLAMES spectra are extending the VD profiles out to more than  $500''$ . This nicely demonstrates that a proper multi-instrument approach is able to provide the VD profile of Galactic GCs over the entire radial extension of each system.

#### 5.4. Systemic Rotation Signals

The spatial distribution of the surveyed stars in the plane of the sky is symmetric with respect to the cluster center out to a maximum distance ( $d_{\max}$ ) that varies from one system to another, but is always larger than twice the half-mass-radius ( $r_h$ ). This allowed us to search for evidence of systemic rotation over a significant portion of the radial extension of each cluster.

For this purpose, we used the method fully described in Bellazzini et al. (2012). In short, we considered a line passing through the cluster center with position angle (PA) varying from  $0^\circ$  (north direction) to  $180^\circ$  (south direction), by steps of  $10^\circ$  and with  $90^\circ$  direction corresponding to the east. For each value of PA, such a line splits the observed sample in two. If the cluster is rotating along the line of sight, we expect to find a value of PA that maximizes the difference between the median RVs of the two

subsamples ( $\Delta \tilde{V}_{\text{med}}$ ), since one component is mostly approaching, while the other is receding with respect to the observer. Moving PA from this value has the effect of gradually decreasing the difference in median RV. Hence, the appearance of a coherent sinusoidal behavior of  $\Delta \tilde{V}_{\text{med}}$  as a function of PA is a signature of rotation and its best-fit sine function provides an estimate of the rotation amplitude ( $A_{\text{rot}}$ ) and the position angle of the cluster rotation axis ( $\text{PA}_0$ ). In the presence of systemic rotation, the stellar distribution in a diagram showing the measured RVs ( $\tilde{V}_r$ ) as a function of the projected distances from the rotation axis (XR) shows an asymmetry, with two diagonally opposite quadrants being more populated than the remaining two. In combination with these diagrams, we also used three different estimators to quantify the statistical significance of any detected signal. We performed a Kolmogorov–Smirnov test to quantify the probability that the RV distributions of the two subsamples on each side of the rotation axis (i.e., one having positive values of the rotated coordinate XR, the other one having  $\text{XR} < 0$ ) are extracted from the same parent distribution. We then used both the Student’s t-test and a Maximum-Likelihood approach for assessing the statistical significance of the difference between the two sample means. The first method has the advantage of being nonparametric, while the other two assume that the data have normal distributions (which is reasonable for samples of stellar RVs in a GC).

To investigate the presence of ordered motions, we considered only the stars used to determine the VD profile (i.e., we neglected



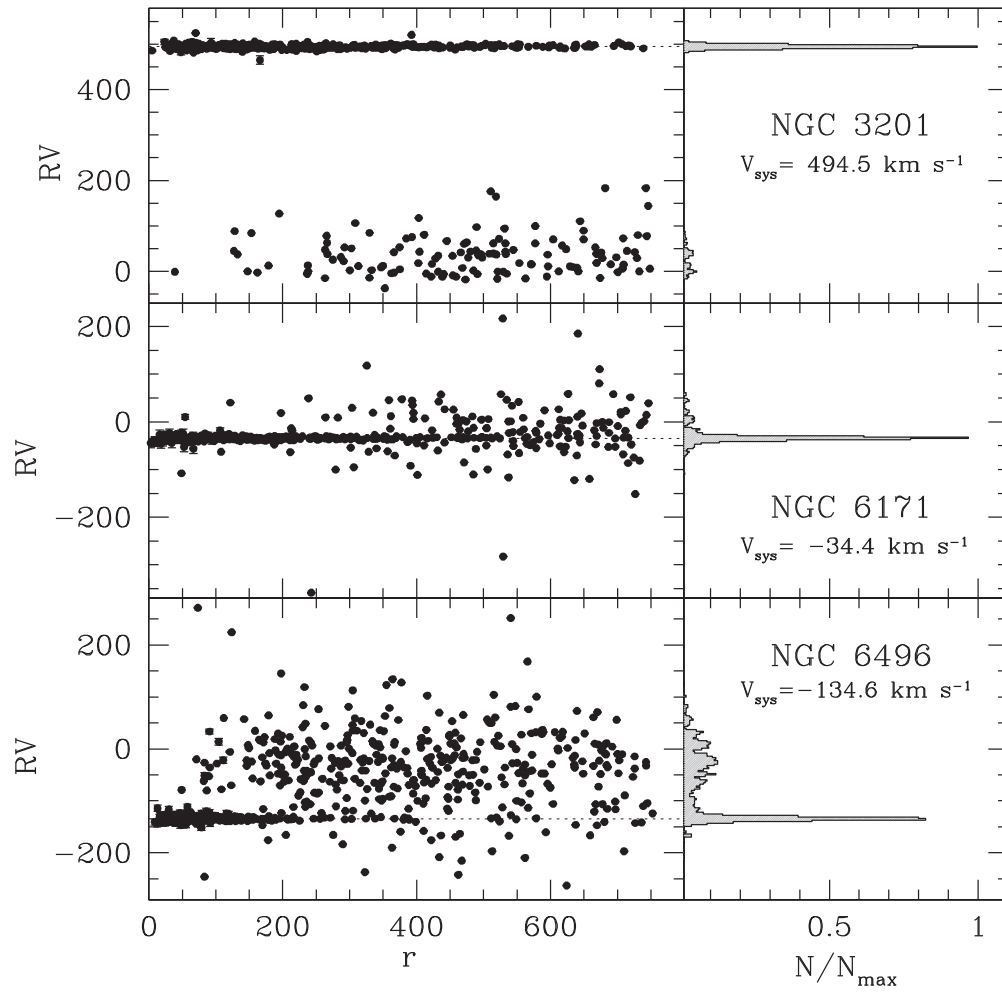


**Figure 4.** As in Figure 2, but for NGC 3201, NGC 6171, and NGC 6496.

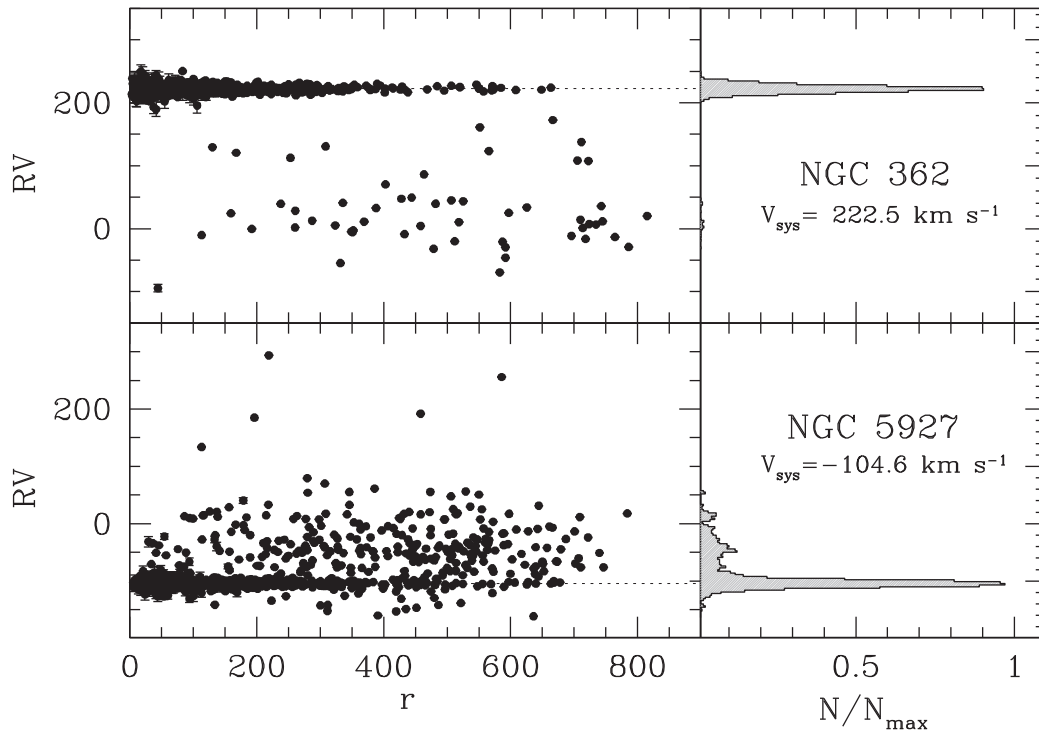


**Figure 5.** As in Figure 2, but for NGC 362 and NGC 5927.

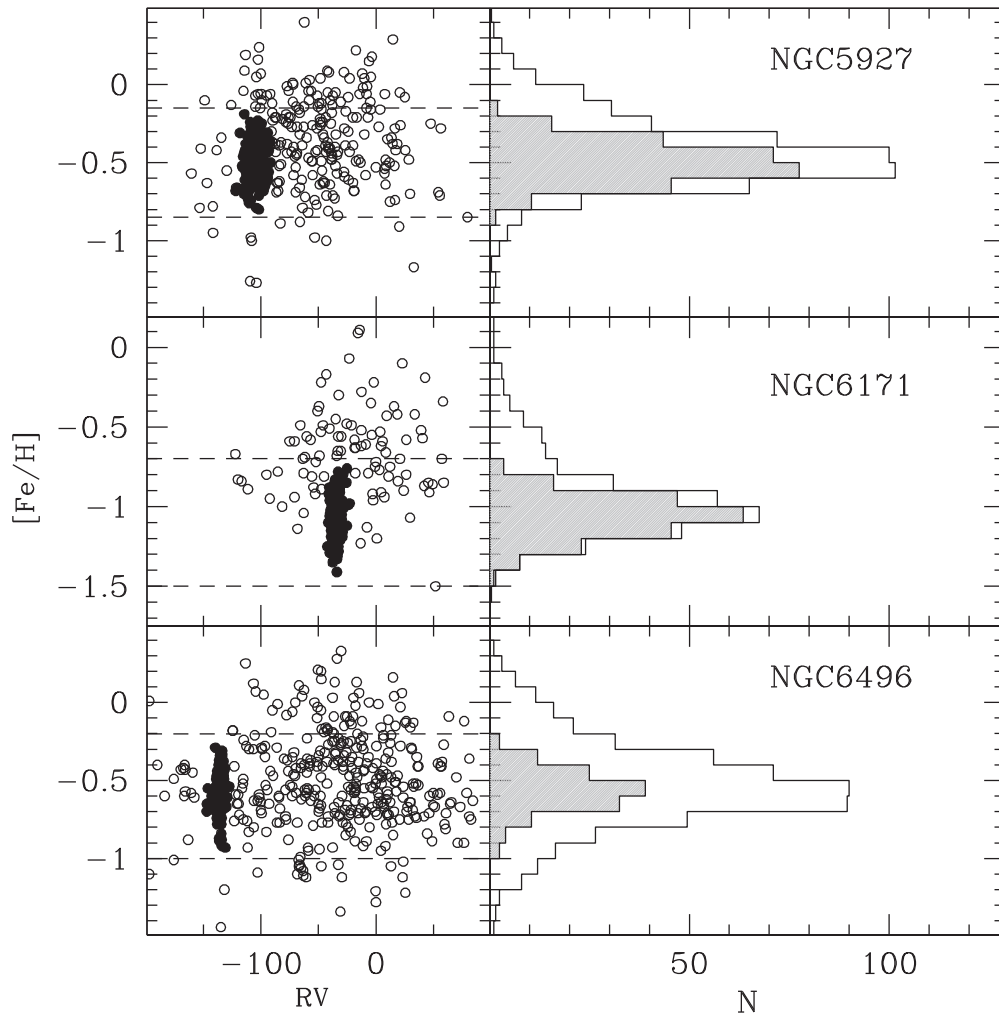


**Figure 6.**  $[\text{Fe}/\text{H}]$  abundance ratios as a function of radial velocities (left panels) and corresponding metallicity distributions (right panels) for the targets observed with the HR21 grating of FLAMES in the three clusters with pronounced Galactic field contamination. In each panel, the range of cluster metallicities is delimited by the two dashed lines. The targets with the highest probability to be cluster members are plotted as filled circles and their corresponding metallicity histogram is shaded in gray.

**Table 4**  
Systemic Velocity and Central VD of the Program Clusters

| Cluster  | $V_{\text{sys}}$<br>( $\text{km s}^{-1}$ ) | $\sigma_0$<br>( $\text{km s}^{-1}$ ) | $V_{\text{sys,H}}$<br>( $\text{km s}^{-1}$ ) | $\sigma_{0,\text{H}}$<br>( $\text{km s}^{-1}$ ) |
|----------|--|--------------------------------------|--|---|
| NGC 288  | $-44.6 \pm 0.4$                            | $3.0 \pm 0.3$                        | $-45.4 \pm 0.2$                              | $2.9 \pm 0.3$                                   |
| NGC 362  | $222.5 \pm 0.4$                            | $8.8 \pm 1.6$                        | $223.5 \pm 0.5$                              | $6.4 \pm 0.3$                                   |
| NGC 1261 | $71.6 \pm 0.6$                             | $5.5 \pm 0.4$                        | $68.2 \pm 4.6$                               | ...   |
| NGC 1904 | $205.4 \pm 0.6$                            | $5.9 \pm 0.7$                        | $205.8 \pm 0.4$                              | $5.3 \pm 0.4$                                   |
| NGC 3201 | $494.5 \pm 0.4$                            | $4.5 \pm 0.5$                        | $494.0 \pm 0.2$                              | $5.0 \pm 0.2$                                   |
| NGC 5272 | $-147.2 \pm 0.4$                           | $7.2 \pm 0.7$                        | $-147.6 \pm 0.2$                             | $5.5 \pm 0.3$                                   |
| NGC 5927 | $-104.6 \pm 0.4$                           | $6.7 \pm 0.7$                        | $-107.5 \pm 0.9$                             | ...   |
| NGC 6171 | $-34.4 \pm 0.5$                            | $3.8 \pm 0.4$                        | $-34.1 \pm 0.3$                              | $4.1 \pm 0.3$                                   |
| NGC 6254 | $75.8 \pm 0.4$                             | $6.0 \pm 0.5$                        | $75.2 \pm 0.7$                               | $6.6 \pm 0.8$                                   |
| NGC 6496 | $-134.6 \pm 0.7$                           | $3.2 \pm 0.4$                        | $-112.7 \pm 5.7$                             | ...   |
| NGC 6723 | $-95.3 \pm 0.4$                            | $5.0 \pm 0.4$                        | $-94.5 \pm 3.6$                              | ...   |

**Note.** Systemic velocity ( $V_{\text{sys}}$ ) and central VD as determined in the present work (columns 2 and 3, respectively), and as quoted in the Harris (1996) catalog (last two columns).

all the outliers and field contaminants excluded from the previous analysis, and for the three most contaminated GCs we limited the search to distances with negligible field contamination). We searched for rotation signals over each system as a whole, and also

in discrete radial bins out to the maximum distance allowed  $d_{\text{max}}$ . In the case of weak rotation, this should allow us to detect at least the maximum of the signal (i.e., the rotational velocity peak), which is expected to be at some nonvanishing distance from the rotation axis. While no significant evidence of global rotation has been found when the stars observed over the entire cluster extension are considered, in all cases we were able to identify the radial region with the strongest rotation signal. The results are summarized in Figures 9–12 and in Table 6.<sup>12</sup> Indications of

<sup>12</sup> Note that the probabilities and significance levels listed in Table 6 could be slightly overestimated because the statistical rejection of the null hypothesis (no rotation) is more likely when multiple hypotheses are tested (in our approach, we searched for rotation signatures in a few radial intervals per cluster). A way to take this into account (Bonferroni 1936) is to multiply the KS probabilities listed in Table 6 by the number of bins surveyed (see the last column of the table). However, given the small number of bins used and the high-significance level of the detected signals, this correction does not significantly alter our results. On the other hand, the crude application of the Bonferroni correction to this scientific case is not completely appropriate, since the probability of detecting rotation is not the same in all radial bins. In fact, the amplitude of the rotation curve is expected to have a maximum (hence to be more easily detectable) at some off-centered radius (see, e.g., Figure 10 in Kacharov et al. 2014 and Figure 3 in Tiongco et al. 2017), and the application of the Bonferroni approach possibly over-corrects (artificially decreases) the significance of the detections in this case.

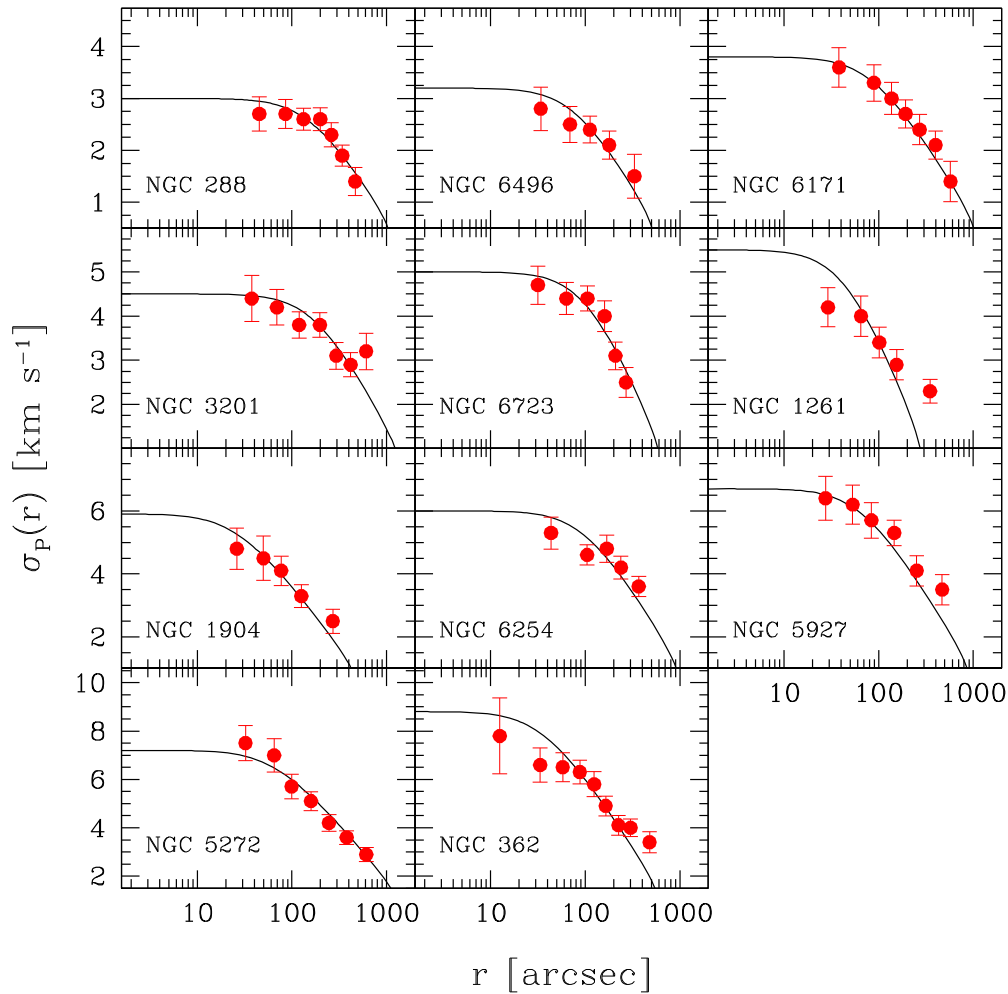


**Figure 7.** Projected velocity dispersion profiles for the program clusters as determined from the RV of individual stars surveyed with KMOS+FLAMES observations (red filled circles). The solid lines correspond to the projected VD profiles of the King models that best fit the observed density/surface brightness distributions (see Section 5.3).

systemic rotation have been found in the majority of the GCs in our sample. The most significant (at more than  $3\sigma$ ) signals are detected in six cases (NGC 288, NGC 362, NGC 1904, NGC 3201, NGC 5272, and NGC 6171), while we estimate an  $\sim 2\sigma$  statistical significance for NGC 1261 (although the number of stars is relatively small), NGC 5927, NGC 6496, and NGC 6723, and there is no evidence of systemic rotation in NGC 6254.

## 6. Discussion

We presented the first results obtained from the MIKIS survey from the analysis of  $\sim 6275$  high/medium resolution spectra of individual stars sampling the entire radial extension of 11 GGCs. This data set allowed us to accurately determine the systemic velocity and VD profile, and to investigate the presence of ordered rotation in each system. In particular, we provided the first determination of the internal kinematical properties of NGC 1261 and NGC 6496.

For the majority of the clusters, the derived systemic velocities are in very good agreement with the results published in the literature (see Table 4 for the comparison with the values quoted in the Harris 1996 catalog; see also Lane et al. 2010, Kimmig et al. 2015, Lardo et al. 2015). The only notable exception is NGC 6496, for which we find a difference of

$\sim 20 \text{ km s}^{-1}$  with respect to the value quoted in the Harris catalog. This can be explained by noticing that the latter is determined from very few (less than 10) RV measures only (the most recent source being Rutledge et al. 1997, who acquired four spectra in this cluster), while we used more than 100 stars. We can thus confidently conclude that the systemic velocity quoted here for NGC 6496 is the most accurate and reliable so far.

The MIKIS survey collections of RVs provide a symmetric sampling of the plane of the sky around each cluster center, out to  $\sim 2\text{--}7 r_h$  depending on the system. We have thus been able to search for signatures of systemic rotation over a significant radial portion of each GC, finding that the majority of the targets (9 over 11) show evidence of rotation at intermediate cluster-centric distances (see Table 6). This is in agreement with the findings of Kamann et al. (2018), who, from the analysis of MUSE spectra, concluded that  $\sim 60\%$  of the GCs in their sample presents some degree of internal rotation. The data set presented here offers the advantage of a significantly larger spatial coverage. In fact, for the three clusters in common (NGC 362, NGC 3201, and NGC 6254), the MUSE observations cover 1, 0.5, and  $0.8 r_h$ , respectively, while our data extend much further out (to  $\sim 5.4$ ,  $3.2$ , and  $3.2 r_h$ ,

**Table 5**  
VD Profiles of the Program Clusters

| NGC 288           |                   |                   |     |                                     |  |
|-------------------|-------------------|-------------------|-----|-------------------------------------|--|
| $r_i$<br>(arcsec) | $r_e$<br>(arcsec) | $r_m$<br>(arcsec) | $N$ | $\sigma_p$<br>(km s <sup>-1</sup> ) | err $_{\sigma}$<br>(km s <sup>-1</sup> ) |
| 15.00             | 65.00             | 45.12             | 39  | 2.70                                | 0.33                                     |
| 65.00             | 105.00            | 85.49             | 64  | 2.70                                | 0.28                                     |
| 105.00            | 165.00            | 132.62            | 86  | 2.60                                | 0.21                                     |
| 165.00            | 235.00            | 199.32            | 83  | 2.60                                | 0.22                                     |
| 235.00            | 295.00            | 261.11            | 57  | 2.30                                | 0.23                                     |
| 295.00            | 395.00            | 339.94            | 62  | 1.90                                | 0.20                                     |
| 395.00            | 645.00            | 465.92            | 28  | 1.40                                | 0.27                                     |
| NGC 362           |                   |                   |     |                                     |  |
| $r_i$<br>(arcsec) | $r_e$<br>(arcsec) | $r_m$<br>(arcsec) | $N$ | $\sigma_p$<br>(km s <sup>-1</sup> ) | err $_{\sigma}$<br>(km s <sup>-1</sup> ) |
| 3.00              | 20.00             | 12.49             | 33  | 7.80                                | 1.57                                     |
| 20.00             | 45.00             | 33.37             | 70  | 6.60                                | 0.71                                     |
| 45.00             | 70.00             | 57.79             | 65  | 6.50                                | 0.60                                     |
| 70.00             | 110.00            | 87.53             | 88  | 6.30                                | 0.49                                     |
| 110.00            | 140.00            | 124.19            | 64  | 5.80                                | 0.52                                     |
| 140.00            | 200.00            | 164.43            | 73  | 4.90                                | 0.41                                     |
| 200.00            | 260.00            | 223.99            | 50  | 4.10                                | 0.41                                     |
| 260.00            | 350.00            | 300.89            | 65  | 4.00                                | 0.36                                     |
| 350.00            | 700.00            | 478.30            | 35  | 3.40                                | 0.43                                     |
| NGC 1261          |                   |                   |     |                                     |  |
| $r_i$<br>(arcsec) | $r_e$<br>(arcsec) | $r_m$<br>(arcsec) | $N$ | $\sigma_p$<br>(km s <sup>-1</sup> ) | err $_{\sigma}$<br>(km s <sup>-1</sup> ) |
| 1.00              | 50.00             | 29.15             | 107 | 4.20                                | 0.44                                     |
| 50.00             | 80.00             | 65.11             | 59  | 4.00                                | 0.46                                     |
| 80.00             | 130.00            | 101.61            | 57  | 3.40                                | 0.35                                     |
| 130.00            | 200.00            | 155.01            | 39  | 2.90                                | 0.34                                     |
| 200.00            | 800.00            | 349.32            | 37  | 2.30                                | 0.27                                     |
| NGC 1904          |                   |                   |     |                                     |  |
| $r_i$<br>(arcsec) | $r_e$<br>(arcsec) | $r_m$<br>(arcsec) | $N$ | $\sigma_p$<br>(km s <sup>-1</sup> ) | err $_{\sigma}$<br>(km s <sup>-1</sup> ) |
| 5.00              | 40.00             | 26.13             | 39  | 4.80                                | 0.65                                     |
| 40.00             | 60.00             | 49.94             | 28  | 4.50                                | 0.70                                     |
| 60.00             | 100.00            | 76.89             | 42  | 4.10                                | 0.47                                     |
| 100.00            | 170.00            | 125.62            | 41  | 3.30                                | 0.36                                     |
| 170.00            | 600.00            | 270.13            | 23  | 2.50                                | 0.38                                     |
| NGC 3201          |                   |                   |     |                                     |  |
| $r_i$<br>(arcsec) | $r_e$<br>(arcsec) | $r_m$<br>(arcsec) | $N$ | $\sigma_p$<br>(km s <sup>-1</sup> ) | err $_{\sigma}$<br>(km s <sup>-1</sup> ) |
| 20.00             | 50.00             | 37.62             | 39  | 4.40                                | 0.52                                     |
| 50.00             | 90.00             | 69.42             | 59  | 4.20                                | 0.40                                     |
| 90.00             | 150.00            | 119.05            | 84  | 3.80                                | 0.30                                     |
| 150.00            | 250.00            | 197.37            | 99  | 3.80                                | 0.28                                     |
| 250.00            | 350.00            | 293.92            | 64  | 3.10                                | 0.30                                     |
| 350.00            | 500.00            | 417.33            | 66  | 2.90                                | 0.27                                     |
| 500.00            | 800.00            | 608.31            | 43  | 3.20                                | 0.41                                     |
| NGC 5272          |                   |                   |     |                                     |  |
| $r_i$<br>(arcsec) | $r_e$<br>(arcsec) | $r_m$<br>(arcsec) | $N$ | $\sigma_p$<br>(km s <sup>-1</sup> ) | err $_{\sigma}$<br>(km s <sup>-1</sup> ) |
| 1.00              | 50.00             | 32.31             | 99  | 7.50                                | 0.72                                     |
| 50.00             | 80.00             | 64.86             | 69  | 7.00                                | 0.69                                     |
| 80.00             | 120.00            | 99.09             | 72  | 5.70                                | 0.51                                     |
| 120.00            | 200.00            | 158.67            | 110 | 5.10                                | 0.39                                     |

**Table 5**  
(Continued)

| NGC 288           |                   |                   |     |                                     |  |
|-------------------|-------------------|-------------------|-----|-------------------------------------|--|
| $r_i$<br>(arcsec) | $r_e$<br>(arcsec) | $r_m$<br>(arcsec) | $N$ | $\sigma_p$<br>(km s <sup>-1</sup> ) | err $_{\sigma}$<br>(km s <sup>-1</sup> ) |
| 200.00            | 300.00            | 246.19            | 83  | 4.20                                | 0.35                                     |
| 300.00            | 500.00            | 378.94            | 91  | 3.60                                | 0.28                                     |
| 500.00            | 770.00            | 610.01            | 53  | 2.90                                | 0.29                                     |
| NGC 5927          |                   |                   |     |                                     |  |
| $r_i$<br>(arcsec) | $r_e$<br>(arcsec) | $r_m$<br>(arcsec) | $N$ | $\sigma_p$<br>(km s <sup>-1</sup> ) | err $_{\sigma}$<br>(km s <sup>-1</sup> ) |
| 1.00              | 40.00             | 27.49             | 96  | 6.40                                | 0.70                                     |
| 40.00             | 70.00             | 53.18             | 109 | 6.20                                | 0.62                                     |
| 70.00             | 100.00            | 83.96             | 67  | 5.70                                | 0.56                                     |
| 100.00            | 200.00            | 146.35            | 129 | 5.30                                | 0.40                                     |
| 200.00            | 300.00            | 252.78            | 56  | 4.10                                | 0.48                                     |
| 300.00            | 800.00            | 469.22            | 56  | 3.50                                | 0.48                                     |
| NGC 6171          |                   |                   |     |                                     |  |
| $r_i$<br>(arcsec) | $r_e$<br>(arcsec) | $r_m$<br>(arcsec) | $N$ | $\sigma_p$<br>(km s <sup>-1</sup> ) | err $_{\sigma}$<br>(km s <sup>-1</sup> ) |
| 2.00              | 65.00             | 38.12             | 72  | 3.60                                | 0.38                                     |
| 65.00             | 110.00            | 89.06             | 54  | 3.30                                | 0.35                                     |
| 110.00            | 160.00            | 136.78            | 51  | 3.00                                | 0.31                                     |
| 160.00            | 220.00            | 192.80            | 59  | 2.70                                | 0.27                                     |
| 220.00            | 320.00            | 271.18            | 39  | 2.40                                | 0.29                                     |
| 320.00            | 500.00            | 399.60            | 34  | 2.10                                | 0.27                                     |
| 500.00            | 750.00            | 574.61            | 10  | 1.40                                | 0.39                                     |
| NGC 6254          |                   |                   |     |                                     |  |
| $r_i$<br>(arcsec) | $r_e$<br>(arcsec) | $r_m$<br>(arcsec) | $N$ | $\sigma_p$<br>(km s <sup>-1</sup> ) | err $_{\sigma}$<br>(km s <sup>-1</sup> ) |
| 1.00              | 70.00             | 43.52             | 85  | 5.30                                | 0.51                                     |
| 70.00             | 140.00            | 104.48            | 114 | 4.60                                | 0.32                                     |
| 140.00            | 200.00            | 168.63            | 73  | 4.80                                | 0.43                                     |
| 200.00            | 280.00            | 238.30            | 73  | 4.20                                | 0.36                                     |
| 280.00            | 550.00            | 367.07            | 70  | 3.60                                | 0.32                                     |
| NGC 6496          |                   |                   |     |                                     |  |
| $r_i$<br>(arcsec) | $r_e$<br>(arcsec) | $r_m$<br>(arcsec) | $N$ | $\sigma_p$<br>(km s <sup>-1</sup> ) | err $_{\sigma}$<br>(km s <sup>-1</sup> ) |
| 8.00              | 50.00             | 33.85             | 62  | 2.80                                | 0.42                                     |
| 50.00             | 85.00             | 68.93             | 60  | 2.50                                | 0.35                                     |
| 85.00             | 140.00            | 111.90            | 62  | 2.40                                | 0.26                                     |
| 140.00            | 250.00            | 178.99            | 37  | 2.10                                | 0.27                                     |
| 250.00            | 450.00            | 330.70            | 13  | 1.50                                | 0.42                                     |
| NGC 6723          |                   |                   |     |                                     |  |
| $r_i$<br>(arcsec) | $r_e$<br>(arcsec) | $r_m$<br>(arcsec) | $N$ | $\sigma_p$<br>(km s <sup>-1</sup> ) | err $_{\sigma}$<br>(km s <sup>-1</sup> ) |
| 5.00              | 50.00             | 31.56             | 112 | 4.70                                | 0.43                                     |
| 50.00             | 80.00             | 63.22             | 87  | 4.40                                | 0.36                                     |
| 80.00             | 140.00            | 105.47            | 130 | 4.40                                | 0.28                                     |
| 140.00            | 180.00            | 159.86            | 71  | 4.00                                | 0.35                                     |
| 180.00            | 240.00            | 208.16            | 58  | 3.10                                | 0.31                                     |
| 240.00            | 320.00            | 269.32            | 29  | 2.50                                | 0.34                                     |

**Note.** The table lists the internal and external radius of each radial bin ( $r_i$  and  $r_e$ , respectively), average cluster-centric distance of the member stars in the bin ( $r_m$ ), number of stars in the bin ( $N$ ), measured VD, and its uncertainty in the bin ( $\sigma_p$  and  $\text{err}_{\sigma}$ , respectively).



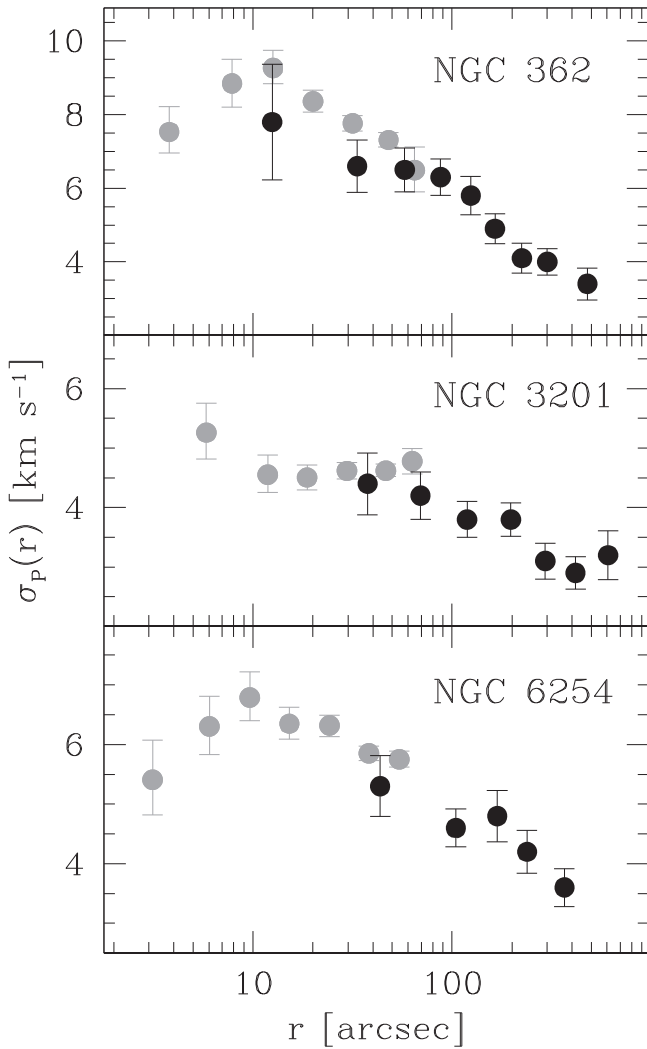


**Figure 8.** Projected VD profile of the three clusters in common with Kamann et al. (2018). Filled black circles are from this work, while the gray circles are the results of Kamann et al. (2018).

respectively). Kamann et al. (2018) found no signatures of rotation in the latter two GCs, while a marginal signal was detected in the center (at  $\sim 0.05r_h$ ) of NGC 362. We confirm the absence of rotation in NGC 6254, and we find strong signatures both in NGC 3201 (at  $\sim 2r_h$ ) and in NGC 362 (at  $4.2r_h$ ). These results, however, are not in disagreement, since our detections are well outside the regions sampled by the MUSE observations of Kamann et al. (2018). Detailed comparisons with other previous works in the literature are not straightforward because global rotation amplitudes, determined all over the radial range sampled by the observations, are usually quoted. However, we can note that, in agreement with our results, some signatures of systemic rotation were already detected in NGC 288, NGC 362, NGC 1904, NGC 5272, and NGC 6171 (see Lane et al. 2010; Scarpa et al. 2011; Bellazzini et al. 2012; Kimmig et al. 2015; Lardo et al. 2015, and references therein).

The observations collected so far (this paper, and, e.g., van den Bosch et al. 2006; Bellazzini et al. 2012; Fabricius et al. 2014; Kacharov et al. 2014; Kimmig et al. 2015; Bellini et al. 2017; Boberg et al. 2017; Kamann et al. 2018) seem to suggest that, when properly surveyed, the majority of GCs

shows some signature of systemic rotation at intermediate distances from the center. In addition, rotation has been found in both intermediate-age (Davies et al. 2011; Mackey et al. 2013) and young massive (Hénault-Brunet et al. 2012) clusters. On the theoretical side, a number of studies predict that massive star clusters are born with significant amounts of rotation, which is gradually dissipated via the effects of angular momentum transport and loss due to the effects of two-body relaxation and star escape (see, e.g., Longaretti & Lagoute 1996; Einsel & Spurzem 1999; Fiestas et al. 2006; Ernst et al. 2007; Varri & Bertin 2012; Hong et al. 2013; Vesperini et al. 2014; Mapelli 2017; Tiongco et al. 2017). The recent  $N$ -body simulations of Tiongco et al. (2017) discuss the long-term evolution of GC rotational properties after an initial violent relaxation phase (Vesperini et al. 2014) and show that at the end of that epoch the radial profile of the cluster rotation velocity displays a well-defined peak at a few half-mass radii in all the explored models. The combined effect of angular momentum transport and angular momentum loss due to the escape of stars leads to a progressive decline in the magnitude of the peak of the rotation curve with time (see their Figure 4). The peak is initially located at a few  $r_h$ , and it then moves slightly inward over time, but remains essentially located in a region between 0.5 and  $2.5 r_h$  for most of the cluster’s evolution (see their Figure 6). According to Tiongco et al. (2017) the amplitude of the rotation peak is expected to decrease as a function of time by one order of magnitude, from typical values of  $\sim 0.5\sigma_0$ , down to  $\sim 0.05\sigma_0$  in the most evolved systems (see their Figure 7). Although a detailed comparison between simulations and observations is beyond the scope of this study, we find a general overall agreement with the predictions of Tiongco et al. (2017), both in terms of the ratio between  $A_{\text{rot}}$  and  $\sigma_0$  (which ranges between 0.1 and 0.3 in our candidate rotators) and for what concerns the radial location of the rotation peak (which is found within a few  $r_h$  in our observations; see Table 6).

For the candidate rotators, the rotation amplitudes are of the order of  $\sim 1\text{--}2 \text{ km s}^{-1}$  (see Table 6). In principle, these should be taken into account for the determination of the true stellar VD that is defined as the square root of  $\sigma_P^2(r) - A_{\text{rot}}^2(r)$ , where  $\sigma_P(r)$  is the observed root mean square of the RV distribution determined in Section 5.3 (see Table 5). In practice, however, the ratio between  $A_{\text{rot}}(r)$  and  $\sigma_P(r)$  in the radial bin where the maximum rotation signal is found is always of the order of  $\sim 0.3\text{--}0.4$  and the resulting value of the true VD coincides within the errors with the measured values of  $\sigma_P(r)$ . Hence, we can safely adopt  $\sigma_P(r)$  as the true VD profiles of each cluster, with no real need of corrections for ordered rotation.

As shown in Figure 7, the derived VD profiles sample a significant radial fraction of each cluster, covering from 3 up to 20 half-mass radii. As expected for “well-behaved” GCs, the stellar VD profile declines outward. Indeed, the King (1966) models that best fit the observed density/luminosity distribution of each cluster also reproduce the projected VD profiles reasonably well (see the solid lines in Figure 7). The adopted model parameters are listed in Table 7. For NGC 6496, the values quoted in Harris (1996) and in McLaughlin & van der Marel (2005) seem to be affected by some problem (for instance, the half-mass-radius almost coincides with the core radius in the former, while the dimensionless central potential is  $W_0 = 0.3^{+4.3}_{-0.0}$  in the latter). We therefore used the photometric data of the ACS Survey of GGCs

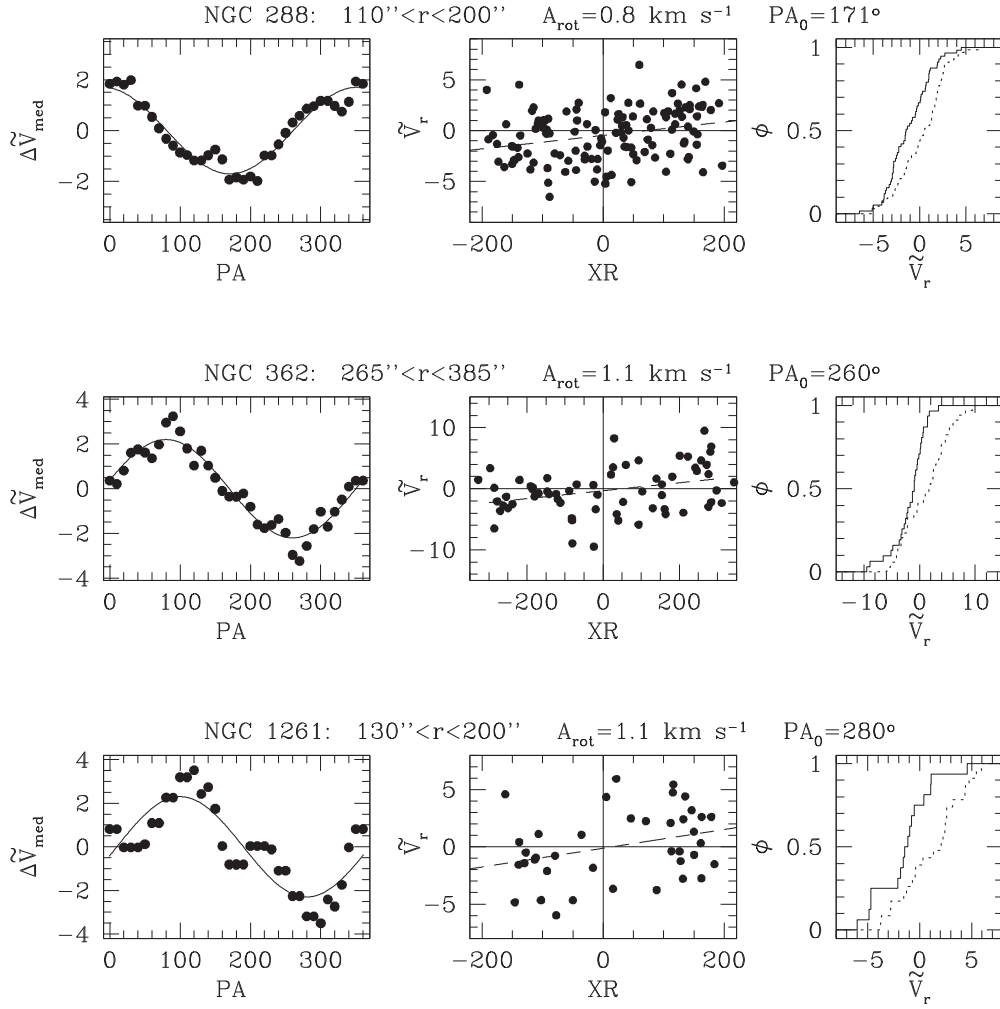


**Figure 9.** Diagnostic diagrams of the rotation signature detected in NGC 288, NGC 362, and NGC 1261 (top, middle, and bottom rows, respectively). For each system, the left panel shows the difference between the median RVs on each side of the cluster with respect to a line passing through the center with a given position angle (PA), as a function of PA itself (see Section 5.4). The continuous line is the sine function that best fits the observed pattern. The best-fit rotation amplitude and position angle ( $A_{\text{rot}}$  and  $PA_0$ , respectively) are labeled above the panels, together with the considered radial range. The central panel shows the distribution of the measured RVs ( $\tilde{V}_r = V_r - V_{\text{sys}}$ ) as a function of the projected distances from the rotation axis (XR) in arcseconds. The dashed line is the least square fit to the data. The right panel shows the cumulative RV distributions for the sample of stars with  $XR < 0$  (solid line) and for that with  $XR > 0$  (dotted line).

(Sarajedini et al. 2007) and 2MASS (Skrutskie et al. 2006) to obtain a new determination of the projected density distribution of NGC 6496 from resolved star counts. The structural parameters of the King model that best fits the resulting profile are  $W_0 = 5.7$  (corresponding to concentration  $c = 1.18$ ), core radius  $r_c = 35''.6$ , and half-mass-radius  $r_h = 93''.6$ . As shown in Figure 7, this model nicely reproduces also the observed VD profile. Particularly interesting is the case of NGC 288, for which we detect a clear decline beyond  $r \sim 200''$  (corresponding roughly to 9 pc for the distance quoted in Ferraro et al. 1999; see Table 7). This is not in agreement with the results of Hernandez et al. (2017), who find that the VD profile of this cluster flattens at  $r \sim 8\text{--}10$  pc and stays constant at  $\sigma_P \simeq 2.0 \text{ km s}^{-1}$  over the whole radial range sampled. It is worth noting, however, that the VD curve of Hernandez et al. (2017) is obtained from 148 stars with cluster-centric distances  $r \leq 16$  pc, while our results are based on a sample of more than 400 members observed out to  $\sim 30$  pc. On the other hand, the observed declining shape of the VD profile is in agreement with the results of Lane et al. (2010) and Kimmig et al. (2015), and it is well matched by the King model that best fits the star density distribution of the cluster.

The King model profiles shown in Figure 7 provide zeroth-order estimates of the central VD ( $\sigma_0$ ) in each cluster. These are listed in Table 4, together with the values quoted in the Harris catalog for comparison. The two sets of values are in good agreement for all the GCs in common, with the exceptions of NGC 362 and NGC 5272 (M3) for which we find significantly larger central VDs. Our results, however, are in good agreement with those recently determined by Kimmig et al. (2015) and Kamann et al. (2018), while the values quoted in the Harris catalog derive from early determinations based on much smaller samples of spectra. Within the uncertainties, our central VDs also agree with those of Lane et al. (2010) and Bellazzini et al. (2012) for the clusters in common. For NGC 5927, instead, we find a lower value ( $6.7 \pm 0.7 \text{ km s}^{-1}$ ) with respect to Lardo et al. (2015), who quote  $\sigma_0 = 11.0 \pm 2.0 \text{ km s}^{-1}$ . This can be explained by noticing that the latter value has been derived from the central extrapolation of a poorly sampled VD profile (79 stars in total, with just  $\sim 5$  objects within  $60''$  from the center), while we have 534 members in total, of which almost 200 are located at  $r < 60''$ .

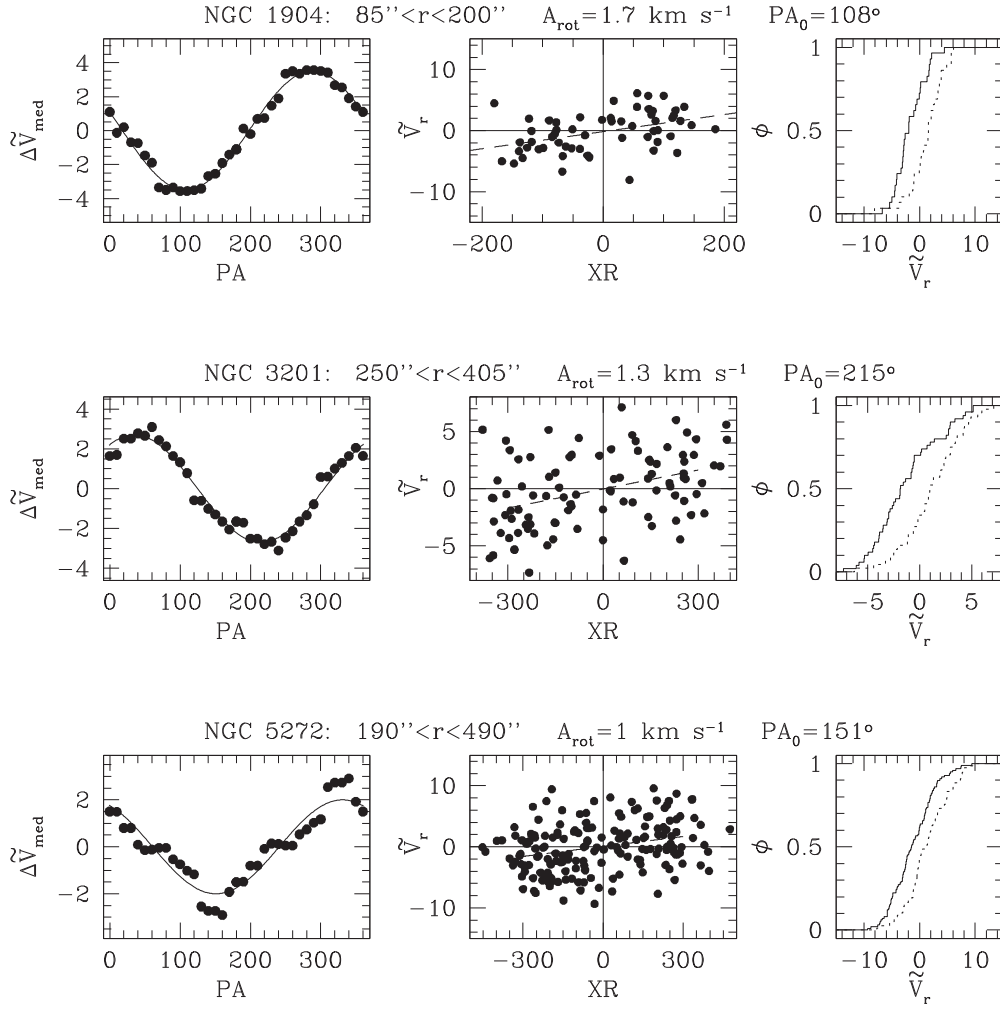


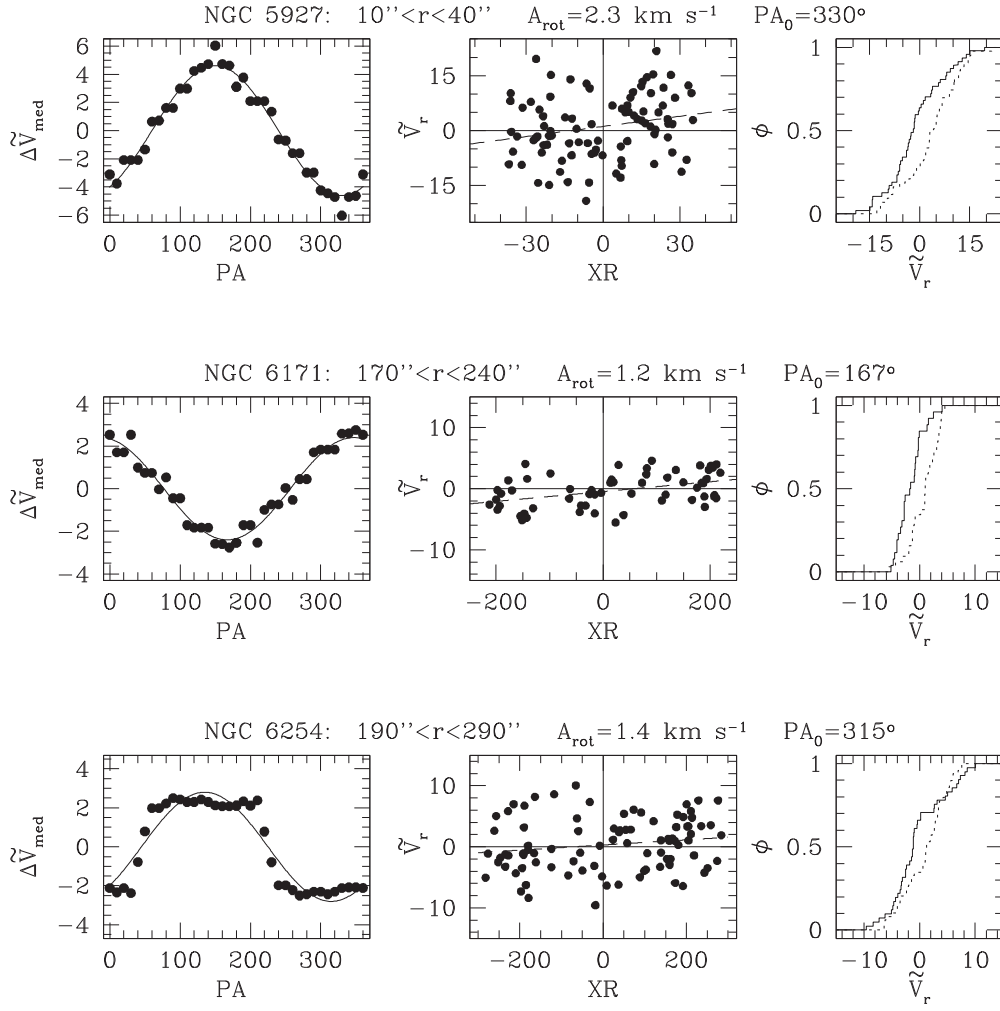
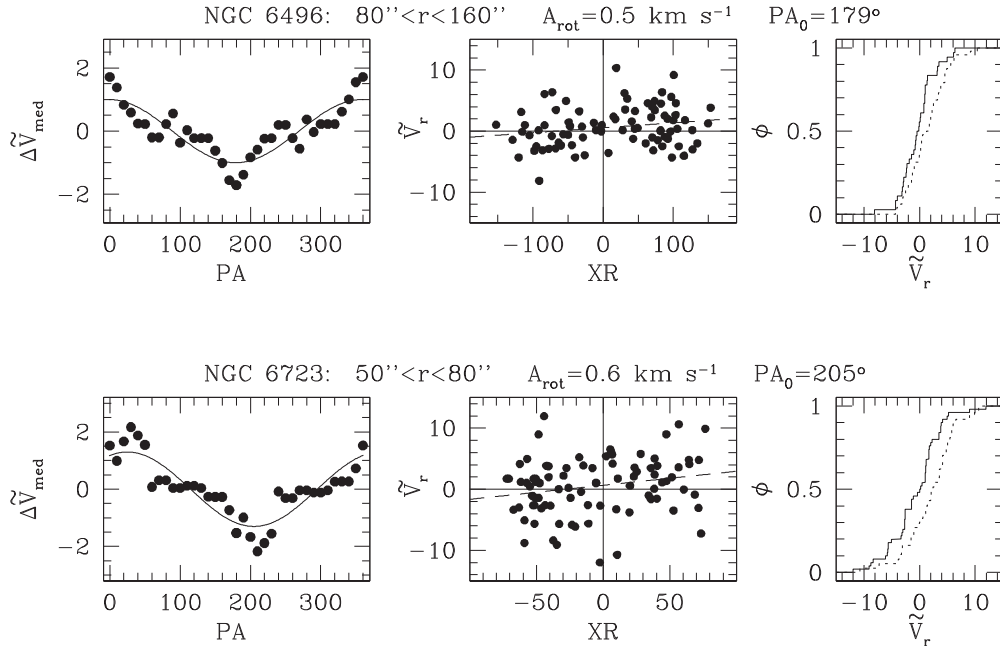
**Figure 10.** As in Figure 9, but for NGC 1904, NGC 3201, and NGC 5272.

Under the assumption that the program clusters are well represented by single-mass, spherical, isotropic, and nonrotating King (1966) models, we can use the derived values of the central VD to estimate the total mass of each system. For this purpose, we use Equation (3) in Majewski et al. (2003), where the parameters  $\mu$  and  $\beta$  have been determined, respectively, by following Djorgovski (1993) and by assuming  $\beta = 1/\sigma_0$  (as appropriate for models with  $W_0 > 5$ ; see the discussion in Richstone & Tremaine 1986). The resulting masses are listed in Table 8. They agree within a factor of  $\sim 2$  with the values quoted in the literature (see Table 8 and also Lane et al. 2010; Zocchi et al. 2012; Kimmig et al. 2015). This is well acceptable if one takes into account all the uncertainties and the fact that the various estimates have been obtained through different methods (for instance, McLaughlin & van der Marel 2005 use total luminosities and population-synthesis V-band mass-to-light ratio ratios, while Baumgardt 2017 uses multimass  $N$ -body simulations).

## 7. Summary and Conclusions

This work is part of the MIKis survey, a project aimed at providing the line-of-sight kinematic information along the entire radial extension of a selected sample of 30 GGCs. To this

purpose, we exploit large and homogeneous data sets of RVs, measured from medium-high resolution spectra of individual stars acquired through the combined use of three ESO-VLT spectrographs: diffraction-limited IF observations with SINFONI for the innermost cluster regions, and KMOS and FLAMES data for the intermediate and external radial ranges, respectively. Here we presented the first results obtained for 11 GGCs in the survey. We provide the first determinations of the VD profile and systemic rotation information for NGC 1261 and NGC 6496. For the latter, we also present updated structural parameters, obtained from the construction of a new density profile from resolved star counts and its King (1966) model best fit. All the observed VD profiles decline outward and, at a first approximation, they are reproduced by the same King model that best fits the density/luminosity distribution. We found evidence of rotation at  $1\text{--}2 r_h$  in the majority of the surveyed clusters. Together with other findings in the literature, this suggests that possibly most (if not all) GGCs display some degree of internal rotation, which might be the remnant of a much larger amount of ordered motions imprinted at birth and then gradually dissipated via two-body relaxation (e.g., Fiestas et al. 2006; Tiongco et al. 2017). Hence, particular care should be devoted to explore the rotational properties of GGCs, since the detection of even weak signals is not an indication of the

**Figure 11.** As in Figure 9, but for NGC 5927, NGC 6171, and NGC 6254.**Figure 12.** As in Figure 9, but for NGC 6496 and NGC 6723.



**Table 6**  
Strongest Rotation Signatures Detected in the Surveyed Clusters

| Cluster  | $d_{\max}$ | $r_i$ | $r_e$ | $r_m$  | $N$ | $A_{\text{rot}}$ | $PA_0$ | $P_{\text{KS}}$      | $P_{\text{Stud}}$ | $n\text{-}\sigma_{\text{ML}}$ | $N_{\text{bin}}$ |
|----------|------------|-------|-------|--------|-----|------------------|--------|----------------------|-------------------|-------------------------------|------------------|
| NGC 288  | 400        | 110   | 200   | 151.20 | 123 | 0.8              | 171    | $1.9 \times 10^{-3}$ | >99.0             | 3.8                           | 3                |
| NGC 362  | 400        | 265   | 385   | 309.20 | 65  | 1.1              | 260    | $9.8 \times 10^{-4}$ | >99.8             | 3.5                           | 8                |
| NGC 1261 | 200        | 130   | 200   | 155.70 | 39  | 1.1              | 280    | $1.0 \times 10^{-2}$ | >99.0             | 2.4                           | 6                |
| NGC 1904 | 200        | 85    | 200   | 124.60 | 58  | 1.7              | 108    | $1.3 \times 10^{-3}$ | >99.8             | 5.1                           | 3                |
| NGC 3201 | 600        | 250   | 405   | 320.40 | 94  | 1.3              | 215    | $9.0 \times 10^{-5}$ | >99.8             | 4.3                           | 5                |
| NGC 5272 | 750        | 190   | 490   | 305.80 | 177 | 1.0              | 151    | $1.5 \times 10^{-4}$ | >99.8             | 4.6                           | 4                |
| NGC 5927 | 100        | 10    | 40    | 28.10  | 90  | 2.3              | 330    | $2.3 \times 10^{-3}$ | >95.0             | 2.0                           | 3                |
| NGC 6171 | 500        | 170   | 240   | 199.60 | 58  | 1.2              | 167    | $8.0 \times 10^{-4}$ | >99.8             | 3.8                           | 5                |
| NGC 6254 | 450        | 190   | 290   | 235.30 | 90  | 1.4              | 315    | $4.2 \times 10^{-3}$ | < 90.0            | 1.5                           | 5                |
| NGC 6496 | 200        | 80    | 160   | 116.40 | 84  | 0.5              | 179    | $1.5 \times 10^{-2}$ | >95.0             | 3.0                           | 4                |
| NGC 6723 | 200        | 50    | 80    | 63.40  | 87  | 0.6              | 205    | $6.8 \times 10^{-3}$ | >99.0             | 2.5                           | 4                |

**Note.** The table lists the maximum distance out to which rotation has been studied ( $d_{\max}$ ), the internal and external radii of each radial bin ( $r_i$  and  $r_e$ , respectively), the mean radius and the number of the stars in the bin used to determine the rotation ( $r_m$  and  $N$ , respectively), the rotation amplitude ( $A_{\text{rot}}$ ) and the position angle of the rotation axis ( $PA_0$ ) in the bin, the Kolmogorov–Smirnov probability that the two samples on each side of the rotation axis are drawn from the same parent distribution ( $P_{\text{KS}}$ ), the t-student probability that the two RV samples have different means ( $P_{\text{Stud}}$ ), the significance level (in units of  $n\text{-}\sigma$ ) that the two means are different following a maximum-likelihood approach ( $n\text{-}\sigma_{\text{ML}}$ ), and the number of radial bins used to search for rotation signals ( $N_{\text{bin}}$ ).

**Table 7**  
Structural Parameters of the Best Fit King Models

| Cluster  | $W_0$ | $c$  | $r_0$ | $r_c$ | $r_h$  | dist  |
|----------|-------|------|-------|-------|--------|-------|
| NGC 288  | 5.80  | 1.21 | 76.56 | 70.0  | 190.00 | 8.83  |
| NGC 362  | 7.65  | 1.73 | 13.52 | 13.0  | 73.84  | 8.63  |
| NGC 1261 | 5.60  | 1.16 | 23.16 | 21.0  | 40.80  | 15.70 |
| NGC 1904 | 7.75  | 1.76 | 9.76  | 9.4   | 56.66  | 13.37 |
| NGC 3201 | 6.15  | 1.29 | 84.22 | 78.0  | 186.00 | 4.97  |
| NGC 5272 | 8.05  | 1.85 | 23.47 | 22.7  | 166.70 | 10.14 |
| NGC 5927 | 7.25  | 1.60 | 26.41 | 25.2  | 66.00  | 7.62  |
| NGC 6171 | 7.00  | 1.53 | 35.41 | 33.6  | 103.80 | 6.17  |
| NGC 6254 | 6.60  | 1.41 | 43.66 | 41.0  | 139.90 | 4.74  |
| NGC 6496 | 5.70  | 1.18 | 39.09 | 35.6  | 93.60  | 11.30 |
| NGC 6723 | 5.40  | 1.11 | 55.41 | 49.8  | 91.80  | 8.70  |

**Note.** The table lists the structural parameters of the King model that best fits the observed density/luminosity profile, and cluster distances: King dimensionless potential and concentration parameter ( $W_0$  and  $c$ , respectively), King, core, and half-mass radii in arcseconds ( $r_0$ ,  $r_c$ , and  $r_h$ , respectively), cluster distance in kpc (dist). The structural parameters of NGC 6496 have been newly determined here, while the others are from Miocchi et al. (2013, for NGC 288, NGC 1904, NGC 5272, and NGC 6254), Dalessandro et al. (2013b, for NGC 362), and Harris (1996, for NGC 1261, NGC 3201, NGC 5927, NGC 6171, and NGC 6723). Distances are from Ferraro et al. (1999) if available, otherwise they are from Harris (1996).

**Table 8**  
Total Mass of the Program Clusters

| Cluster  | $M$  | $M_{\text{McLvdM}}$ | $M_{\text{B17}}$ |
|----------|------|---------------------|------------------|
| NGC 288  | 0.78 | 0.74                | 0.88             |
| NGC 362  | 2.44 | 3.39                | 3.21             |
| NGC 1261 | 1.30 | ...                 | ...              |
| NGC 1904 | 1.29 | ...                 | 2.2              |
| NGC 3201 | 1.21 | 1.10                | 1.58             |
| NGC 5272 | 4.10 | 3.80                | 5.0              |
| NGC 5927 | 1.99 | ...                 | 3.45             |
| NGC 6171 | 0.63 | 0.79                | 0.96             |
| NGC 6254 | 1.26 | 1.51                | 2.26             |
| NGC 6496 | 0.55 | 0.575               | ...              |
| NGC 6723 | 1.32 | 1.905               | 1.96             |

**Note.** The table lists the total mass of the program clusters in units of  $10^5 M_{\odot}$  as measured in the present paper ( $M$ ), in McLaughlin & van der Marel (2005,  $M_{\text{McLvdM}}$ ), and in Baumgardt (2017,  $M_{\text{B17}}$ ).

lack of importance of rotation in these systems, but it possibly represents the observational evidence that most of the clusters were born with significant amounts of ordered motions (Tiongco et al. 2017).














The data presented here can now be complemented with observations of the central regions in order to obtain full radial coverage of each cluster. A nice example based on MUSE data (from Kamann et al. 2018) is shown in Figure 8, but an even a better spatial resolution to explore the innermost region of high density GCs can be reached with the enhanced version of MUSE (WFM-AO, which operates under super-seeing conditions down to FWHM  $\sim 0''.4$ ), or by using SINFONI (see Lanzoni et al. 2013). In a series of future papers, we will present the detailed kinematic study of other specific GGCs, performed by exploiting the powerful multi-instrument data set acquired within the MIKIS survey. The kinematic information along the line of sight thus obtained may then be combined with star density profiles (now feasible for most GCs, see Miocchi et al. 2013) and, for selected clusters, also with the structural and kinematic maps on the plane of the sky as obtained from new-generation astrometric data in the central and outer regions, from *HST* and *Gaia*, respectively. Such a rich view of the phase space of these systems will enable a complete dynamical interpretation, by means of state-of-the-art equilibrium and evolutionary models (e.g., Varri & Bertin 2012 and Wang et al. 2016, respectively).

This first exploration of our rich kinematic survey already proves to be of outstanding value, in at least two respects. On the one hand, it coronates the mounting empirical evidence (see references in the previous section) that a new level of sophistication may now be attained in the characterization of the velocity space of GGCs, unveiling an unexpected degree of kinematic richness, which makes them refreshingly novel “phase space laboratories.” On the other hand, it also provides the motivation and the opportunity to deepen the theoretical exploration of a number of fundamental aspects of collisional stellar dynamics, such as the role of angular momentum, orbital anisotropy and their interplay with the external tidal field. A full theoretical understanding and a detailed observational investigation of the complete velocity space of GCs are essential steps toward an appropriate dynamical interpretation

of a number of outstanding puzzles of this class of stellar systems, especially related to their elusive stellar populations and putative intermediate-mass black holes.

We thank the anonymous referee for useful comments that contributed to improve the presentation of the paper. F.R.F. acknowledges the ESO Visitor Programme for the support and the warm hospitality at the ESO Headquarters in Garching (Germany) during the period when part of this work was performed. A.L.V. acknowledges support from a Marie Skłodowska-Curie Fellowship (MSCA-IF-EFRI 658088).

### ORCID iDs

F. R. Ferraro  <https://orcid.org/0000-0002-2165-8528>  
 A. Mucciarelli  <https://orcid.org/0000-0001-9158-8580>  
 B. Lanzoni  <https://orcid.org/0000-0001-5613-4938>  
 C. Pallanca  <https://orcid.org/0000-0002-7104-2107>  
 E. Lapenna  <https://orcid.org/0000-0002-7662-2186>  
 L. Origlia  <https://orcid.org/0000-0002-6040-5849>  
 E. Dalessandro  <https://orcid.org/0000-0003-4237-4601>  
 E. Valenti  <https://orcid.org/0000-0002-6092-7145>  
 G. Beccari  <https://orcid.org/0000-0002-3865-9906>  
 M. Bellazzini  <https://orcid.org/0000-0001-8200-810X>  
 E. Vesperini  <https://orcid.org/0000-0003-2742-6872>  
 A. Varri  <https://orcid.org/0000-0002-6162-1594>  
 A. Sollima  <https://orcid.org/0000-0001-7484-8467>

### References

- Bailyn, C. D. 1995, *ARA&A*, **33**, 133  
 Baumgardt, H. 2017, *MNRAS*, **464**, 2174  
 Baumgardt, H., & Hilker, M. 2018, *MNRAS*, in press (arXiv:1804.08359)  
 Baumgardt, H., Makino, J., & Hut, P. 2005, *ApJ*, **620**, 238  
 Baumgardt, H., & Sollima, S. 2017, *MNRAS*, **472**, 744  
 Beccari, G., Dalessandro, E., Lanzoni, B., et al. 2015, *ApJ*, **814**, 144  
 Bellazzini, M., Bragaglia, A., Carretta, E., et al. 2012, *A&A*, **538**, A18  
 Bellini, A., Anderson, J., van der Marel, R. P., et al. 2014, *ApJ*, **797**, 115  
 Bellini, A., Bianchini, P., Varri, A. L., et al. 2017, *ApJ*, **844**, 167  
 Bellini, A., Vesperini, E., Piotto, G., et al. 2015, *ApJL*, **810**, L13  
 Bianchini, P., Varri, A. L., Bertin, G., & Zocchi, A. 2013, *ApJ*, **772**, 67  
 Boberg, O. M., Vesperini, E., Friel, E. D., Tiongco, M. A., & Varri, A. L. 2017, *ApJ*, **841**, 114  
 Bonferroni, C. E. 1936, *Teoria statistica delle classi e calcolo delle probabilità* (Firenze: Pubblicazioni del R. Istituto Superiore di Scienze Economiche e Commerciali di Firenze), 3  
 Carballo-Bello, J. A., Martínez-Delgado, D., Navarrete, C., et al. 2018, *MNRAS*, **474**, 683  
 Carrera, R., Gallart, C., Pancino, E., & Zinn, R. 2007, *AJ*, **134**, 1298  
 Carretta, E., Bragaglia, A., Gratton, R. G., et al. 2009, *A&A*, **505**, 117  
 Cordero, M. J., Hénault-Brunet, V., Pilachowski, C. A., et al. 2017, *MNRAS*, **465**, 3515  
 Correnti, M., Bellazzini, M., Dalessandro, E., et al. 2011, *MNRAS*, **417**, 2411  
 Da Costa, G. S. 2012, *ApJ*, **751**, 6  
 Dalessandro, E., Ferraro, F. R., Lanzoni, B., et al. 2013a, *ApJ*, **770**, 45  
 Dalessandro, E., Ferraro, F. R., Massari, D., et al. 2013b, *ApJ*, **778**, 135  
 Davies, B., Bastian, N., Gieles, M., et al. 2011, *MNRAS*, **411**, 1386  
 Davoust, E. 1977, *A&A*, **61**, 391  
 Djorgovski, S. 1993, in ASP Conf. Ser. 50, *Structure and Dynamics of Globular Clusters*, ed. S. G. Djorgovski & G. Meylan (San Francisco, CA: ASP), 373  
 Dubath, P., Meylan, G., & Mayor, M. 1997, *A&A*, **324**, 505  
 Einsel, C., & Spurzem, R. 1999, *MNRAS*, **302**, 81  
 Ernst, A., Glaschke, P., Fiestas, J., Just, A., & Spurzem, R. 2007, *MNRAS*, **377**, 465  
 Fabricius, M. H., et al. 2014, *ApJ*, **787**, L26  
 Ferraro, F. R., Beccari, G., Dalessandro, E., et al. 2009, *Natur*, **462**, 1028  
 Ferraro, F. R., Beccari, G., Rood, R. T., et al. 2004, *ApJ*, **603**, 127  
 Ferraro, F. R., Lanzoni, B., Dalessandro, E., et al. 2012, *Natur*, **492**, 393  
 Ferraro, F. R., Lapenna, E., Mucciarelli, A., et al. 2016, *ApJ*, **816**, 70  
 Ferraro, F. R., Messineo, M., Fusi Pecci, F., et al. 1999, *AJ*, **118**, 1738  
 Ferraro, F. R., Montegriffo, P., Origlia, L., & Fusi Pecci, F. 2000, *AJ*, **119**, 1282  
 Fiestas, J., Spurzem, R., & Kim, E. 2006, *MNRAS*, **373**, 677  
 Gieles, M., & Zocchi, A. 2015, *MNRAS*, **454**, 576  
 Harris, W. E. 1996, *AJ*, **112**, 1487, 2010 edition  
 Heggie, D., & Hut, P. 2003, in *The Gravitational Million-Body Problem: A Multidisciplinary Approach to Star Cluster Dynamics*, ed. D. Heggie & P. Hut (Cambridge: Cambridge Univ. Press), 372  
 Heggie, D. C., & Ramamani, N. 1995, *MNRAS*, **272**, 317  
 Hénault-Brunet, V., Gieles, M., Agertz, O., & Read, J. I. 2015, *MNRAS*, **450**, 1164  
 Hénault-Brunet, V., Gieles, M., Evans, C. J., et al. 2012, *A&A*, **545**, L1  
 Hernandez, X., Cortés, R. A. M., & Scarpa, R. 2017, *MNRAS*, **464**, 2930  
 Hernandez, X., Jiménez, M. A., & Allen, C. 2013, *MNRAS*, **428**, 3196  
 Hong, J., Kim, E., Lee, H. M., & Spurzem, R. 2013, *MNRAS*, **430**, 2960  
 Husser, T.-O., Kamann, S., Dreizler, S., et al. 2016, *A&A*, **588**, A148  
 Ibata, R., Bellazzini, M., Chapman, S. C., et al. 2009, *ApJL*, **699**, L169  
 Ibata, R., Sollima, A., Nipoti, C., et al. 2011, *ApJ*, **743**, 43  
 Jeffreson, S. M. R., Sanders, J. L., Evans, N. W., et al. 2017, *MNRAS*, **469**, 4740  
 Kacharov, N., Bianchini, P., Koch, A., et al. 2014, *A&A*, **567**, A69  
 Kamann, S., Husser, T.-O., Dreizler, S., et al. 2018, *MNRAS*, **473**, 5591  
 Kimmig, B., Seth, A., Ivans, I. L., et al. 2015, *AJ*, **149**, 53  
 King, I. R. 1966, *AJ*, **71**, 64  
 Kuzma, P. B., Da Costa, G. S., & Mackey, A. D. 2018, *MNRAS*, **473**, 2881  
 Kuzma, P. B., Da Costa, G. S., Mackey, A. D., & Roderick, T. A. 2016, *MNRAS*, **461**, 3639  
 Lane, R. R., Kiss, L. L., Lewis, G. F., et al. 2010, *MNRAS*, **406**, 2732  
 Lanzoni, B., Dalessandro, E., Ferraro, F. R., et al. 2007a, *ApJ*, **663**, 267  
 Lanzoni, B., Ferraro, F. R., Alessandrini, E., et al. 2016, *ApJL*, **833**, L29  
 Lanzoni, B., Ferraro, F. R., Dalessandro, E., et al. 2010, *ApJ*, **717**, 653  
 Lanzoni, B., Mucciarelli, A., Origlia, L., et al. 2013, *ApJ*, **769**, 107  
 Lanzoni, B., Sanna, N., Ferraro, F. R., et al. 2007b, *ApJ*, **663**, 1040  
 Lapenna, E., Mucciarelli, A., Ferraro, F. R., et al. 2015a, *ApJ*, **813**, 97  
 Lapenna, E., Origlia, L., Mucciarelli, A., et al. 2015b, *ApJ*, **798**, 23  
 Lardo, C., Pancino, E., Bellazzini, M., et al. 2015, *A&A*, **573**, A115  
 Longaretti, P.-Y., & Lagoute, C. 1996, *A&A*, **308**, 453  
 Lützgendorf, N., Kissler-Patig, M., Gebhardt, K., et al. 2013, *A&A*, **552**, A49  
 Lützgendorf, N., Kissler-Patig, M., Noyola, E., et al. 2011, *A&A*, **533**, A36  
 Mackey, A. D., Da Costa, G. S., Ferguson, A. M. N., & Yong, D. 2013, *ApJ*, **762**, 65  
 Majewski, S. R., Skrutskie, M. F., Weinberg, M. D., & Ostheimer, J. C. 2003, *ApJ*, **599**, 1082  
 Mandushev, G., Staneva, A., & Spasova, N. 1991, *A&A*, **252**, 94  
 Mapelli, M. 2017, *MNRAS*, **467**, 3255  
 Martin, N. F., Ibata, R. A., Chapman, S. C., Irwin, M., & Lewis, G. F. 2007, *MNRAS*, **380**, 281  
 Mashchenko, S., & Sills, A. 2005, *ApJ*, **619**, 258  
 Massari, D., Mucciarelli, A., Ferraro, F. R., et al. 2014, *ApJ*, **791**, 101  
 McLaughlin, D. E., & van der Marel, R. P. 2005, *ApJS*, **161**, 304  
 Meylan, G., & Heggie, D. C. 1997, *A&ARv*, **8**, 1  
 Mocchi, P. 2007, *MNRAS*, **381**, 103  
 Mocchi, P., Lanzoni, B., Ferraro, F. R., et al. 2013, *ApJ*, **774**, 151  
 Olszewski, E. W., Saha, A., Knezek, P., et al. 2009, *AJ*, **138**, 1570  
 Pasquini, L., Avila, G., Allaert, E., et al. 2000, *Proc. SPIE*, **4008**, 129  
 Peñarubia, J., Varri, A. L., Breen, P. G., Ferguson, A. M. N., & Sánchez-Janssen, R. 2017, *MNRAS*, **471**, L31  
 Piotto, G., Milone, A. P., Bedin, L. R., et al. 2015, *AJ*, **149**, 91  
 Pryor, C., & Meylan, G. 1993, in ASP Conf. Ser. 50, *Structure and Dynamics of Globular Clusters*, ed. S. G. Djorgovski & G. Meylan (San Francisco, CA: ASP), 357  
 Richer, H. B., Heyl, J., Anderson, J., et al. 2013, *ApJL*, **771**, L15  
 Richstone, D. O., & Tremaine, S. 1986, *AJ*, **92**, 72  
 Rutledge, G. A., Hesser, J. E., Stetson, P. B., et al. 1997, *PASP*, **109**, 883  
 Sarajedini, A., Bedin, L. R., Chaboyer, B., et al. 2007, *AJ*, **133**, 1658  
 Sbordone, L., Bonifacio, P., Castelli, F., & Kurucz, R. L. 2004, *MSAIS*, **5**, 93  
 Scarpa, R., Marconi, G., Carraro, G., Falomo, R., & Villanova, S. 2011, *A&A*, **525**, A148  
 Sharples, R., Bender, R., Agudo Berbel, A., et al. 2010, *Msngr*, **139**, 24  
 Shin, J., Kim, S. S., & Lee, Y.-W. 2013, *JKAS*, **46**, 173  
 Skrutskie, M. F., Cutri, R. M., Stiening, R., et al. 2006, *AJ*, **131**, 1163  
 Sollima, A., Bellazzini, M., & Lee, J.-W. 2012, *ApJ*, **755**, 156  
 Sollima, A., Bellazzini, M., Smart, R. L., et al. 2009, *MNRAS*, **396**, 2183  
 Sollima, A., Ferraro, F. R., Lovisi, L., et al. 2016, *MNRAS*, **462**, 1937  
 Sommariva, V., Piotto, G., Rejkuba, M., et al. 2009, *A&A*, **493**, 947

- Tiongco, M. A., Vesperini, E., & Varri, A. L. 2017, [MNRAS](#), **469**, 683
- Tonry, J., & Davis, M. 1979, [AJ](#), **84**, 1511
- Trager, S. C., Djorgovski, S., & King, I. R. 1993, in ASP Conf. Ser. 50, Structure and Dynamics of Globular Clusters, ed. S. G. Djorgovski & G. Meylan (San Francisco, CA: ASP), 347
- Valenti, E., Ferraro, F. R., & Origlia, L. 2007, [AJ](#), **133**, 1287
- Valenti, E., Ferraro, F. R., Perina, S., & Origlia, L. 2004, [A&A](#), **419**, 139
- van den Bosch, R., de Zeeuw, T., Gebhardt, K., Noyola, E., & van de Ven, G. 2006, [ApJ](#), **641**, 852
- Varri, A. L., & Bertin, G. 2009, [ApJ](#), **703**, 1911
- Varri, A. L., & Bertin, G. 2012, [A&A](#), **540**, A94
- Vasquez, S., Zoccali, M., Hill, V., et al. 2015, [A&A](#), **580**, 121
- Vesperini, E., McMillan, S. L. W., D'Antona, F., & D'Ercole, A. 2013, [MNRAS](#), **429**, 1913
- Vesperini, E., & Trenti, M. 2010, [ApJL](#), **720**, L179
- Vesperini, E., Varri, A. L., McMillan, S. L. W., & Zepf, S. E. 2014, [MNRAS](#), **443**, L79
- Walker, M. G., Mateo, M., Olszewski, E. W., et al. 2006, [AJ](#), **131**, 2114
- Wang, L., Spurzem, R., Aarseth, S., et al. 2016, [MNRAS](#), **458**, 1450
- Watkins, L. L., van der Marel, R. P., Bellini, A., & Anderson, J. 2015, [ApJ](#), **803**, 29
- Wilson, C. P. 1975, [AJ](#), **80**, 175
- Zocchi, A., Bertin, G., & Varri, A. L. 2012, [A&A](#), **539**, A65
- Zocchi, A., Gieles, M., & Hénault-Brunet, V. 2017, [MNRAS](#), **468**, 4429